Hydrodynamics of the Yukawa One Component Plasma

Contact *james.mithen@physics.ox.ac.uk*

Author 1 J. P. Mithen

University of Oxford, Clarendon Laboratory, Parks Road, Oxford, OX1 3PU

Author 2 J. Daligault

Theoretical Division, Los Alamos National Laboratory, Los Alamos, NM, 87545, USA

Author 3 G. Gregori

University of Oxford, Clarendon Laboratory, Parks Road, Oxford, OX1 3PU

Introduction

The hydrodynamic description is a very common starting point for investigating a wide range of basic and complex physical phenomena in fluids. In this macroscopic context, the behaviour of the fluid is governed by the equations of fluid mechanics [1] (e.g. the Navier-Stokes equations). These equations give a wide range of physical predictions (hydrodynamic modes, etc.) that are frequently tested and verified experimentally (e.g. [2]).

From a microscopic standpoint, usually the hydrodynamic regime or *hydrodynamic limit* corresponds to wavenumbers k such that $kl_f \ll 1$ with l_f the 'mean free path' and frequencies ω such that $\omega\tau_c \ll 1$ with τ_c the 'mean collision time'. These conditions, which are already rather qualitative for a system governed by uncorrelated binary collisions, become even more indeterminate when many-body correlations are present because the concepts of 'mean free path' and 'mean collision time' cease to have a clear physical meaning. Thus, when these many-body correlations are present (as is the case, for example, in a liquid or dense plasma), the rather general question of the domain of validity of the hydrodynamic limit is particularly challenging. The extent to which these correlations are present in the system depends on the thermodynamic parameters - the density and temperature - as well as the strength and range of the (microscopic) interactions. For instance, one can expect that the hydrodynamic description only applies at lengthscales that are greater than the range r_c of the potential (i.e. $kr_c < 1$) - in other words, that the domain of validity of the hydrodynamic limit will shrink as the range of the potential increases.

In this contribution, we investigate when the hydrodynamic description (rather than a more detailed microscopic description) is applicable for a physical system. To achieve this, we consider the microscopic dynamics of the so-called Yukawa One Component Plasma (YOCP), which has interaction potential $v(r) = q^2 \exp(-r/r_c)/r$, where q^2 is the strength and r_c the range of the potential. Since it is known that this model is fully characterised by two dimensionless parameters [3], we are able to very effectively explore the entire parameter space (density n , temperature T , strength and range of the interaction potential) that influences the applicability of the hydrodynamic description. Specifically, these parameters are the reduced range $r_c^* = r_c/a$, where $a = (4\pi n/3)^{-1/3}$ is (a measure of) the average inter-particle spacing, and the coupling strength $\Gamma = q^2/(ak_bT)$, which itself characterises completely the degree of many body correlations present in the system for a given range. We calculate the complete (equilibrium) microscopic dynamics of this model – specifically, we calculate the so-called dynamical structure factor – and compare these to the dynamics predicted by the hydrodynamic (i.e. macroscopic) description.

Dynamical Structure Factor (DSF)

The space and time dependent density-density correlation function $<n(\boldsymbol{r},t)n(\boldsymbol{r}',t')>$ (also known as the Van Hove function) plays a privileged role in statistical physics as a bridge between theory and experiment. Here $n(\boldsymbol{r},t)$ is the (microscopic) density of a system of N point particles

$$n(\boldsymbol{r},t) = \sum_{i=1}^{N} \delta(\boldsymbol{r} - \boldsymbol{r}_i(t))$$

And $<...>$ denotes the usual statistical (thermal equilibrium) average, which is given for the canonical ensemble as

$$<...> = \frac{1}{Z} \int ... e^{-BH(\boldsymbol{r}^N, \boldsymbol{p}^N)} d\boldsymbol{r}^N d\boldsymbol{p}^N$$

With Z the canonical partition function. Here B is the inverse temperature $1/k_bT$ and $H(\boldsymbol{r}^N, \boldsymbol{p}^N)$ is the Hamiltonian of the system. Working instead with the density fluctuation

$$\delta n(\boldsymbol{r},t) = n(\boldsymbol{r},t) - <n(\boldsymbol{r},t)>$$

The intermediate scattering function is defined as

$$F(\boldsymbol{k},t) = \frac{1}{2\pi N} <\delta n(\boldsymbol{k},t)\delta n(-\boldsymbol{k},t')> \quad (1)$$

Where

$$\delta n(\boldsymbol{k},t) = n(\boldsymbol{k},t) - <n(\boldsymbol{k},t)>$$

is the density fluctuation in wavevector space, with $n(\boldsymbol{k},t) = \sum_{i=1}^{N} e^{-i\boldsymbol{k}\cdot\boldsymbol{r}_i(t)}$ the spatial Fourier transform of the density at time t . Finally then, the Dynamical Structure Factor $S(\boldsymbol{k},\omega)$ is the Fourier transform in time of the intermediate scattering function

$$S(\boldsymbol{k},\omega) = \int_{-\infty}^{\infty} F(\boldsymbol{k},t) e^{i\omega t} dt \quad (2)$$

When the system possesses spherical symmetry (as is the case for the Yukawa model, because the interaction potential depends only on the distance between two particles), the DSF depends only on the magnitude k of the wavevector $\boldsymbol{k}$, and is thus denoted as $S(k,\omega)$ henceforth. The DSF corresponds experimentally to the spectrum measured from light (e.g. x-ray) or neutron inelastic scattering experiments.

Computing the DSF

Determining the DSF is a case of evaluating the integral given in Eq. (2), which requires calculation of the intermediate scattering function. This cannot generally be done analytically – one notable counterexample being an ideal gas of non-interacting particles. Thus, it is usual to resort to numerical methods for the calculation of the DSF. Of use here is the 'ergodicity assumption' (see e.g. [4]) that allows the statistical average to be computed instead as a time average. Roughly

speaking, the 'ergodicity assumption' amounts to the hypothesis that the dynamical system 'samples' the states in the phase space in time with the same frequency as given by the weighting in the statistical average. Specifically, when applied to the calculation of the intermediate scattering function, one writes mathematically

$$F(k,t)=\frac{1}{2\pi N}\lim_{T\to\infty}\frac{1}{T}\int_0^T \delta n(\boldsymbol{k},t+t')\delta n(-\boldsymbol{k},t')dt'$$

In this way knowledge of the dynamics of the system (i.e. the trajectories of the particles as given by Newton's equations for the case of a classical system) allows one to calculate a statistical average of a quantity of physical interest (in this case the intermediate scattering function). Therefore, the problem of calculating the DSF reduces to solving Newton's equations for the particle trajectories, which can be done numerically by taking advantage of the long established techniques that generally come under the umbrella term 'Molecular Dynamics' (MD).

Hydrodynamic Description of the DSF

From MD simulations then the 'exact' DSF for the Yukawa model can be calculated to within numerical accuracy. It is this quantity that we wish to compare to the hydrodynamic description, in order to examine when the hydrodynamic description is applicable. This macroscopic description is determined from the linearised hydrodynamic (Navier-Stokes) equations, which are (e.g. [5])

$$\begin{aligned}\frac{\partial}{\partial t}\delta n(\boldsymbol{r},t)&=-n\nabla\cdot\boldsymbol{v}(\boldsymbol{r},t)\\ mn\frac{\partial \boldsymbol{v}(\boldsymbol{r},t)}{\partial t}&=-\nabla\delta p(\boldsymbol{r},t)+\eta\nabla^2\boldsymbol{v}(\boldsymbol{r},t)+(\zeta+\frac{\eta}{3})\nabla\nabla\cdot\boldsymbol{v}(\boldsymbol{r},t)\\ T\frac{\partial}{\partial t}\delta s(\boldsymbol{r},t)&=\frac{\kappa}{n}\nabla^2\delta T(\boldsymbol{r},t)\end{aligned} \qquad (3)$$

In Eqs. (3), n and T are the equilibrium number density and temperature respectively, with m the particle mass. The shear and bulk viscosities η and ζ enter into the momentum balance equation with the thermal conductivity κ in the energy balance equation. One can express the entropy and pressure fluctuations ($\delta s(\boldsymbol{r},t)$ and $\delta p(\boldsymbol{r},t)$ respectively) in terms of the density and temperature fluctuations ($\delta n(\boldsymbol{r},t)$ and $\delta T(\boldsymbol{r},t)$ respectively) and subsequently solve this system of equations for the density fluctuations. In this way (making use of the definition in Eq. (2)) one obtains the hydrodynamic expression for the dynamical structure factor (e.g. [5],[6])

$$\frac{S(k,\omega)}{S(k)}=\frac{\gamma-1}{\gamma}\frac{2D_T k^2}{\omega^2+(D_T k^2)^2}+\frac{1}{\gamma}\left[\frac{\sigma k^2}{(\omega+c_s k)^2+(\sigma k^2)^2}+\frac{\sigma k^2}{(\omega-c_s k)^2+(\sigma k^2)^2}\right] \qquad (4)$$

In Eq. (4), γ is the ratio of heat capacities (C_v/C_p), $D_T=\kappa/(nC_p)$ is the thermal diffusivity, c_s the adiabatic sound speed, and σ the sound attenuation coefficient defined by

$$\sigma=\frac{1}{2}\left[\frac{(\gamma-1)}{\gamma}\frac{\kappa}{nC_v}+\frac{\frac{4}{3}\eta+\zeta}{nm}\right]$$

Since the entire physics of the Yukawa model depends only on the coupling strength and range, so each of these four unknowns (γ , c_s , σ and D_T) appearing in Eq. (4) are functions of Γ and r_c^* only. Indeed, since the sound speed and heat capacities are known to reasonable accuracy from equation of state calculations [7], and the viscosities and thermal conductivity have also been calculated [8],[9], the macroscopic description of Eq. (4) is effectively known – as required for our study - as a function of k and ω . We note that the equation of state calculations show that $\gamma\approx 1$ for the Γ and r_c^* values of interest here; therefore the hydrodynamic description of the DSF as given in Eq. (4) reduces to a single 'Brillouin' peak whose position in frequency space is given by $\omega=c_s k$ with a height and width that scale as $1/k^2$ and k^2 respectively . It is these predictions of the macroscopic description that we wish to test against the 'exact' DSF as computed with the MD simulations.

Range of Applicability of the Hydrodynamic Description

Fig. 1 shows $S(k,\omega)$ as calculated from MD plotted alongside Eq. (4) for several choices of coupling strength and range.

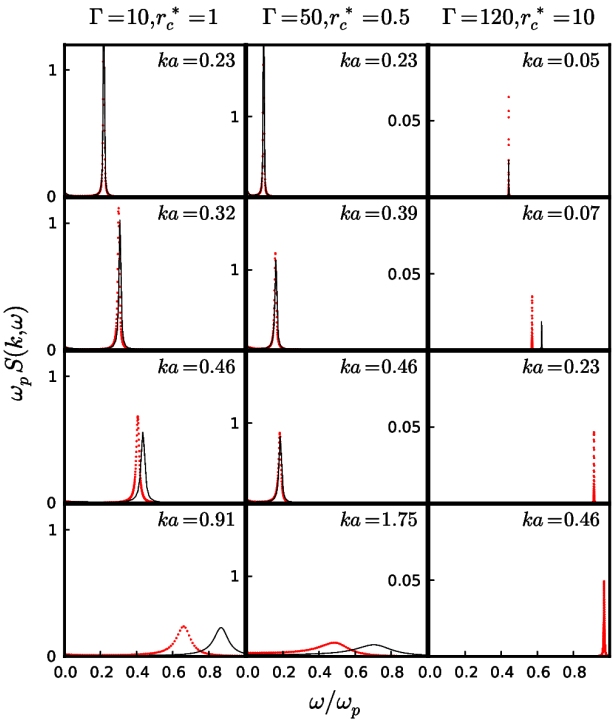

Figure 1: DSF as calculated from MD (red dots) compared with the DSF given by the hydrodynamic description in Eq. (4) (black line) for three different Γ and r_c^* values.

As shown in Fig 1. (top three panels) we find that one can always go to lengthscales sufficiently long (i.e. sufficiently small k) that the hydrodynamic description is valid. We find that rather than requiring conditions on both k and ω , the hydrodynamic description is valid providing $ka<(ka)_{max}$, where $(ka)_{max}$ is the wavenumber beyond which the hydrodynamic description breaks down (i.e. no longer works well). Below $(ka)_{max}$, the hydrodynamic description of $S(k,\omega)$ works very well indeed for all ω - the height, width and position of the Brillouin peak are all predicted accurately. Physically, no condition on ω is required because the system dynamics at sufficiently long lengthscales are always slow enough for the macrosopic equations to be applicable (this is illustrated in Fig 1. - the Brillouin peak is always at small ω for small k). As can also be seen in Fig 1., at k values greater than $(ka)_{max}$ the Brillouin peak is always located at smaller ω than predicted by the hydrodynamic description ($\omega=c_s k$) - this is a well known phenomenon in real liquids (see e.g. [10]). The manner in which the excellent correspondence between the hydrodynamic description and the true microscopic dynamics of the system breaks down is shown for the height and width of the peak in Fig. 2. As seen from Fig. 2, the true height of the DSF

decreases more slowly as k increases than Eq. (4) predicts, and the true width of the DSF also increases more slowly.

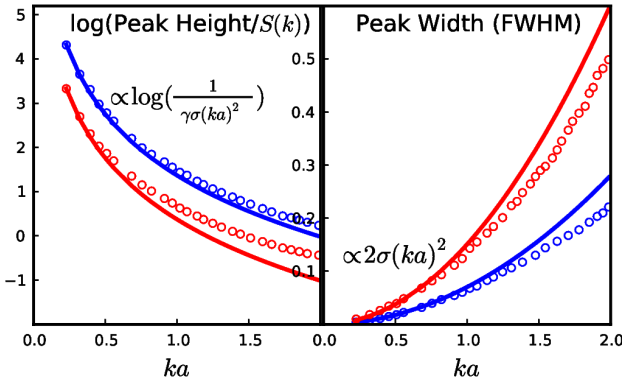

Figure 2: Height and width of Brillouin peak as computed from MD (open circles), and the predictions of the hydrodynamic description (solid lines). Red: $\Gamma=10, r_c^*=0.5$ **, Blue:** $\Gamma=50, r_c^*=0.5$ **.**

By increasing the importance of many body correlations in the system (i.e. increasing Γ) for a specific r_c^* value, we find that $(ka)_{max}$ is not in general significantly changed (not shown) . This is perhaps a slightly surprising result, as the system intuitively becomes more 'collisional' as Γ increases, and one may therefore expect $(ka)_{max}$ to increase with increasing Γ . On the other hand, the range r_c^* is of the utmost consequence to the domain of validity of the hydrodynamic description : the hydrodynamic description is only valid on lengthscales greater than this range. This is most effectively illustrated by looking at the position of the Brillouin peak for a selection of r_c^* values (Fig. 3). As can be seen in Fig. 3, when the interaction potential becomes more long ranged, it is necessary to look at increasingly long lengthscales (small ka) for the hydrodynamic description to be valid.

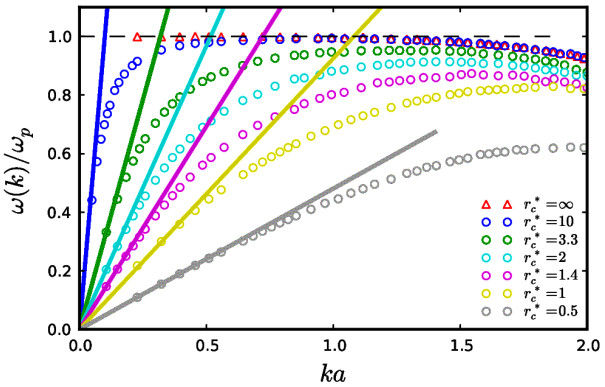

Figure 3: Dependence of the domain of validity of the hydrodynamic description on the range of the potential. The open circles are the MD results for the position of the Brillouin peak, with the associated linear relations (solid lines) $\omega=c_s k$ **also shown for each** r_c^* **value. In all cases** $\Gamma=10$ **.**

Indeed, in terms of the range of the potential rather than the inter-particle spacing, we find from a fit to the MD results the approximate relation

$$(ka)_{max} \sim 0.39 (r_c^*)^{-0.86} \qquad (5)$$

Concluding Remarks

Yukawa potentials are frequently used in dense plasma physics [3]. Recently, it was shown that the use of a Yukawa potential to describe the effective ion-ion interaction, with a range given by the electron-ion screening length in the linear approximation, was able to reproduce well the results of *ab-initio* density functional theory (DFT) simulations [11]. Therefore, within the range of applicability given approximately by Eq. (5), the hydrodynamic description can provide an important complement to DFT techniques, as no dynamical information is available in those simulations.

Acknowledgements

This work was supported by the John Fell Fund and by EPSRC grant no. EP/G007187/1. J. P. Mithen would like to thank the Oxford Supercomputing Centre and the hospitality of the Plasma Theory and Applied Mathematics group at Los Alamos National Laboratory.

References

1. L. D. Landau and E. M. Lifshitz , *Fluid Mechanics*, (Oxford: Pergamon, 1987).
2. T. Scopigno *et. al.*, *Phys. Rev. E*, **65**, 031205 (2002).
3. Z. Donkó *et. al.*, *J. Phys: Condensed Matter*, **20**, 413101 (2008).
4. D. Frenkel and B. Smit, *Understanding Molecular Simulation*, (Elsevier, 1996).
5. J. P. Hansen and I. R. McDonald, *Theory of Simple Liquids*, (Academic Press, 2006).
6. J. P. Boon and S. Yip, *Molecular Hydrodynamics*, (Dover, 1991).
7. S. Hamaguchi *et. al.*, *J. Chem. Phys.*, **105**, 7641 (1996).
8. T. Saigo and S. Hamaguchi, *Phys. Plasmas*, **9**, 1210 (2002).
9. Z. Donkó and P. Hartmann, Phys. Rev. E, **69**, 016405 (2004).
10. U. Balucani and M. Zoppi, *Dynamics of the Liquid State*, (Oxford, 1994).
11. K. Wünsch *et. al.*, *Phys. Rev. E*, **79,** 010201 (2009).

The Accuracy of Rear-Surface Measurements of the Angular-Divergence of a Laser-Generated Fast-Electron Beam

Contact *christopher.ridgers@imperial.ac.uk*

C.P. Ridgers, M. Sherlock, R.G. Evans & R.J. Kingham

Imperial College of Science Technology and Medicine

London, SW7 2AZ

Introduction

The interaction between high-intensity lasers and solid targets is of key importance in fast-ignition inertial confinement fusion [1] and ion-acceleration [2]. Cone-guided fast-ignition uses the interaction between a high-intensity heater beam and the inner tip of a solid gold cone to generate fast-electrons which then go on to heat a compressed pellet of fusion fuel. The angular divergence of the electron beam is critical in determining the flux of fast-electrons reaching the core and so their absorption there. In laser-solid target experiments relevant to this fusion scheme the angular divergence is usually inferred from temperature measurements at the rear-surface or from the size of the ion-emitting region [3-6]. In target-normal sheath ion-acceleration (TNSA), which has potential applications to cancer-therapy, a beam of ions is accelerated by a sheath electric field at the rear-surface. This field has been observed in experiments to spread very rapidly along the target rear-surface, giving a large ion-emitting region [7].

The validity of inferring the angular divergence of the fast-electron beam from rear-surface measurements will be discussed in detail; in particular the temperature measurement will be shown to give a good estimate of the beam divergence only when the re-circulation of electrons (i.e. their reflection by the sheath fields at the target edges causing them to bounce laterally down the target) was suppressed. The size of the ion-spot will be shown to be a very poor way of estimating the divergence.

Simulation results

Solid density plasmas were simulated with the hybrid Vlasov code FIDO [8]; the Vlasov equation was solved for the fast-electrons generated by the high-intensity laser and a fluid treatment used for the cold electrons which made up the target. The Vlasov equation was solved in 4D (x,y,p,θ) for the evolution of the electron distribution function in phase space. A solid aluminium target was simulated, with density $6\times10^{28}m^{-3}$ and a thickness of 10 microns. The laser intensity was $2\times10^{19}Wcm^{-2}$ with an absorption fraction of 0.3. The laser spot was Gaussian with width 3.6 microns. The electron beam was injected moving in the +y-direction. Re-circulating currents could be suppressed by stretching the numerical grid in the -y direction, allowing the fast-electrons to escape.

Fast-electron number density and background temperature profiles are often used to infer the width of the beam. Figure 1 shows that fast-electron refluxing significantly broadens both, but that the fast-electron number density provides a better estimate of the beam size (20 microns). The temperature is broadened by the rapid saturation of the Ohmic heating rate, as illustrated by equation (1). However, when refluxing was suppressed the width of the temperature profile gave a good estimate of that of the beam.

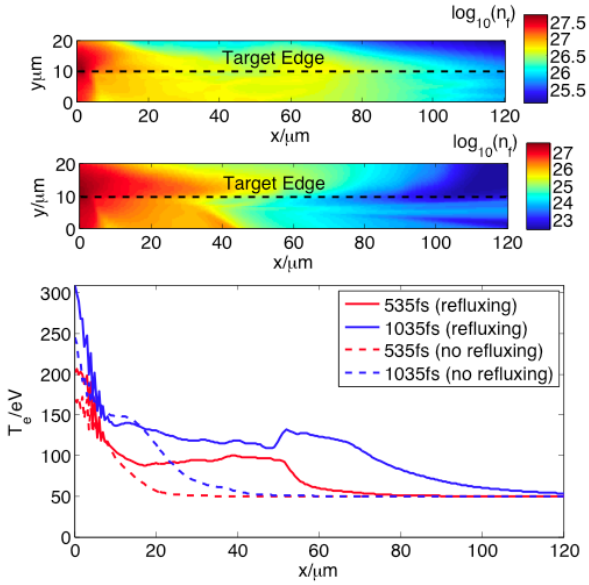

Fig.1: Fast-electron number density after 1035fs with refluxing (top) and without refluxing (middle) after1035fs. Background temperature at the rear-surface (bottom).

$$\frac{\partial T_e}{\partial t} \propto T_e^{-3/2} \qquad (1)$$

When the fast electrons reached the rear surface of the target and entered the vacuum they generated a sheath electric field in the y-direction. Experimentally, sheath fields are seen to move very rapidly along the target's rear surface, therefore there must be a fast-electron current over a large area on the rear-surface. This has so far been explained by re-circulation leading to electrons present far from the injection region.

The width of the sheath region, measured by the width of the ion-emitting region on the rear of the target, yields a very poor measure of the beam divergence due to the insensitivity of the sheath field to the number of incoming electrons. In the simplest model of a sheath the product of the peak electric field (E_y^{peak}) and the sheath width (which is set by the Debye length of the fast-electrons λ_{Df}) must be approximately equal to the average energy of the incoming fast-electrons. It is therefore straightforward to show that the sheath potential (ϕ) is independent of the number density of incoming fast electrons (n_f) and that the peak field scales as $n_f^{1/2}$, as shown in equation (2). This is borne out by the profiles at the rear of the target after 100fs, as shown in figure 2.

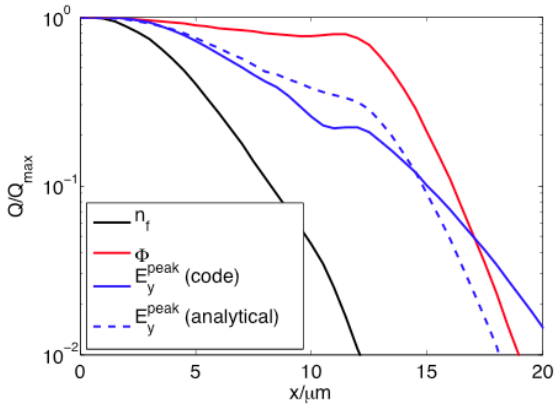

Fig.2: Fast-electron number density, peak sheath field and sheath potential along the target's rear-surface after 100fs, and E_y^{peak} (analytical) $\propto n_f^{1/2}$.

$$E_y^{peak} = \frac{\phi}{\lambda_{Df}} = \phi\left(\frac{e^2}{\varepsilon_0\phi}\right)^{1/2} n_f^{1/2} \qquad (2)$$

The Ampere-Maxwell law gives the rate of growth of the sheath field.

$$\frac{\partial E_y}{\partial t} = -\frac{j_y}{\varepsilon_0} = \frac{e n_f c \cos\theta}{\varepsilon_0} \qquad (3)$$

This can be integrated assuming n_f is constant, until E_y grows so that it may reflect a significant number of fast-electrons. Therefore, in regions of the target where there are few fast-electrons, the sheath field and potential are proportional to n_f. This explains the fall-off of these quantities far from the beam in figure 2.

The speed of expansion can be explained by noting that the insensitivity of the sheath field to n_f meant that relatively low current densities (<1% of the maximum) generated large fields. Initially, the field was generated by electrons on their first pass through the target. In this case the spreading of the sheath field along the rear-surface was due to the difference in arrival times for electrons with different injection angles; those injected at large angles to the target normal had further to go before hitting the rear-surface; this is illustrated in figure 3. In this case the speed of lateral expansion of the sheath field (v_{exp}), assuming the electrons were travelling at the speed of light and that they generated a sheath as soon as they arrived at the rear-surface, is given by equation (4).

$$v_{exp} = \frac{c}{\sin\theta} \qquad (4)$$

Where θ is the angle from the target normal to the position on the rear of the target. Therefore the field expanded super-luminally. Note that this does not violate special relativity; information was not being transferred from the centre of the rear surface to the point at which the sheath had reached but from the injection region to this point at c.

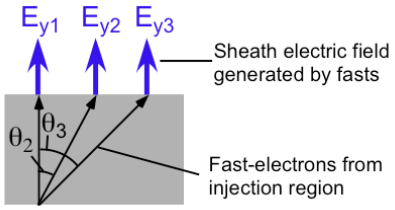

Fig.3: An illustration of the cause of sheath field spreading. At time τ_1 electrons with an incident angle of 0° generate E_{y1}, some time later (τ_2) those with angle θ_2 generate E_{y2}. Finally those with θ_3 generate E_{y3}.

As a corollary, this weak dependence means that it may be possible to increase the efficiency of TNSA ion acceleration by defocusing the beam somewhat in order to scatter the electrons as widely as possible in the target (provided their energy is not curtailed too much by the resultant drop in laser intensity).

Conclusions

Experimental measurements of the angular divergence of fast-electron beams generated in short-pulse laser-solid target interactions may be misleading unless analysed carefully. Although the fast-electron number density was strongly peaked in the region of the beam, re-circulating currents significantly widened the temperature hot-spot on the back. The size of the sheath potential on the back was weakly dependent on the size of the electron beam inside the target and so a measurement of the size of the ion-emitting region gave a very poor estimate of the angular divergence. The sheath field's expansion was controlled by electrons on their first pass through the target and so could expand super-luminally.

Acknowledgements

This work was funded by the HiPER project. We would like to thank Professor Peter Norreys and Robbie Scott for useful discussions.

References

1. M. Tabak *et al*, Phys of Plasmas, **1**, 1626 (1994)
2. S.V. Bulanov & V.S. Khoroshkov, Phys Plasmas, **28**, 453 (2002)
3. K.L. Lancaster *et al*, Phys Rev Lett, **98**, 125002 (2007)
4. J.S. Green *et al*, Phys Rev Lett, **100**, 015003 (2008)
5. K.L. Lancaster *et al*, Phys Rev E, **80**, 045401(R) (2009)
6. M. Zepf *et al*, Phys Rev Lett, **90**, 064801 (2003)
7. P. McKenna *et al*, Phys Rev Lett, **98**, 145001 (2007)
8. M. Sherlock, Phys Plasmas, **16**, 103101 (2009)

High Absorption of Ultra-Intense Laser Pulses in Near Critical Plasmas

Contact *alex.robinson@stfc.ac.uk*

A.P.L.Robinson and R.M.G.M.Trines

Central Laser Facility, STFC Rutherford-Appleton Laboratory, Didcot, Oxfordshire, OX11 0QX

Introduction

Of all the problems that ultra-intense laser-plasma physics is concerned with, the coupling of energy from the laser pulse into the kinetic energy of the plasma particles is perhaps the most important. Attaining efficient coupling is highly important and even critical to a number of prospective applications. Fast Igntion ICF and laser-driven ion acceleration are examples of such applications where coupling efficiency is either a very important or critical issue.

In the work reported here, we analyzed the absorption of 30-100fs, $\lambda \sim 1\mu m$, $a_0 >> 1$ laser pulses in near-critical plasmas. By this we mean plasmas are relativistically transparent and span the density range $0.1n_c < n_e < a_0 n_c$, where n_c is the non-relativistic critical density. The objective of this study is to understand the *gross* properties of these interactions – the propagation velocity of the pulse, the rate of energy absorption, and the scaling of the fast electron energy. This parameter range is particularly interesting as very high absorption (up to 70%) is possible.

Previous Work

The general problem of absorption in underdense plasmas has been the subject of a number of previous studies. Much of this has mainly been concerned with plasmas that are below $0.1n_c$. In this work we have been particularly concerned with Leading Edge Depletion which was originally described in a number of papers (e.g. [1,2]) , but here we make particular reference to the paper by Decker and co-workers [1]. The absorption of laser energy via transverse expulsion of electrons is a concept that is described in a number of papers, see for examples.

The purpose of this work was to re-examine these two concepts – Leading Edge Depletion (LED) and Transverse Ponderomotive Acceleration (TPA) – and to obtain basic analytic models for their gross properties that are good descriptions of what is observed in numerical simulations. Part of this is to determine the answer to an even more fundamental question – are these regimes genuinely distinct at all?

Leading Edge Depletion Theory

Decker et al. give the leading edge propagation velocity as,

$$\frac{u}{c} = 1 - \frac{n_e}{n_c}, \tag{1}$$

in the limit of $n_r << n_c$. The problem with this expression is that in the region $n_c < n_r < a_0 n_c$ one obtains a negative velocity which is at odds with numerical simulations. We set out to derive a better analytic expression by using energy conservation arguments.

In LED absorption notionally occurs at the leading edge by electrons overtaking the leading edge (which travels at a velocity less than c) and taking a momentum of $a_0^2 m_e c/2$ with them. This means that the laser pulse must lose energy at a rate of,

$$\frac{dE}{dt} = -\frac{a_0^2}{2} m_e c^2 n_e u, \tag{2}$$

And the loss of energy manifests as an erosion of the laser field that propagates backwards at velocity v_{er}. These velocities are related via $u = v_g - v_{er}$, where v_g is the group velocity of the laser pulse. This implies that,

$$\frac{dE}{dt} = -\frac{v_{er} I}{c}, \tag{3}$$

where the laser intensity relates to a_0 via $I = a_0^2 m_e c^2 n_c$. Equating 2 and 3 yields the following expression,

$$u = \frac{v_g}{\frac{n_e}{2n_c} + 1}. \tag{4}$$

In the limit of $n_e << n_c$ on retrieves Decker's expression by taking the limit of eqn. 4. In LED the fast electron energy should scale as a_0^2.

Transverse Ponderomotive Acceleration Theory

In 2D and 3D the other route for absorbing energy is transverse ponderomotive expulsion. If we note that each electron expelled will take an energy of $a_0 m_e c^2$ from the laser pulse then we can repeat the LED analysis except with,

$$\frac{dE}{dt} = -a_0 m_e c^2 n_e u, \tag{5}$$

, and obtain the following expression,

$$u = \frac{v_g}{\frac{n_e}{a_0 n_c} + 1}. \tag{6}$$

In TPA, the fast electron energy should scale as a_0.

1D PIC simulations

1D electromagnetic PIC simulations were carried out to validate the theory of LED absorption in 1D. This was done with a 50μm plasma and with a 40fs 'flat-topped' laser pulse that was circularly polarized and had a wavelength of 1μm. In one set of simulations we set $a_0 = 10$ and varied the plasma density over the range $0.5\text{-}2n_c$ and measured the leading edge propagation velocity. In another set, n_e was set to $0.6n_c$, a_0 was varied, and the scaling of the fast electron energy was measured. The results are summarized in figure 1 where we show that eqn. 4 and the a_0^2 scaling of LED are in excellent agreement with the simulation results.

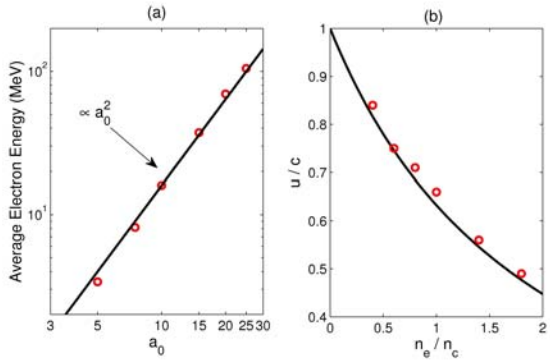

Figure 1. (a) Test of energy scaling in 1D PIC simulation, (b) Test of leading edge propagation velocity in 1D PIC simulation. Black lines correspond to LED analytic results (eqn. 4). Red circles are simulation results.

2D PIC simulations

Next we used 2D PIC simulations using the EPOCH code to study 2D situations where both LED and TPA might occur. In these simulations we also used a 50μm thick plasma and a 'flat-topped' circularly polarized laser pulse. The laser pulse had a Gaussian transverse distribution, characterized by r_L.

We can summarize the results of this investigation by looking at the plots shown in figures 2 and 3.

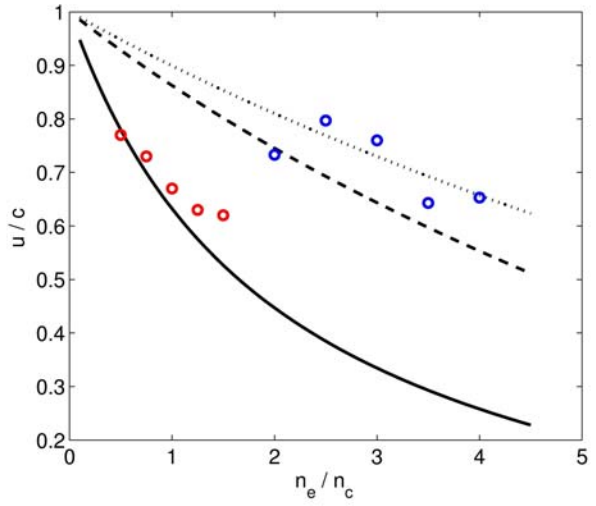

Figure 2. Plot of leading edge velocity, u, from 2D PIC simulations (red circles and blue circles). Both sets have a pulse with a_0 =10 and r_L = 10μm. The solid black line corresponds to eqn. 4 (LED) and the dashed line corresponds to eqn. 6 (TPA). The dotted line corresponds to eqn. 6 (TPA) but with $a_0\sqrt{2}$.

Figure 2 shows the leading edge velocity that was observed over a range of simulations on varying the plasma density. In these two sets, a_0 =10 and r_L = 10μm. Figure 2 shows that the leading edge velocities closely follow either one of the two curves, indicating that there is a LED regime that is well described by the analytic model and a TPA regime that is also well described by the analytic model. The intensity correction included by the dotted line in figure 2 is put there because of intensity increases due to the strong filamentation of the laser pulse that occurs in the TPA regime. Figure 2 also shows that the two regimes are *distinct*, i.e. one does not really observe an admixture of the two, except for regions where there is a smooth transition between the two regimes.

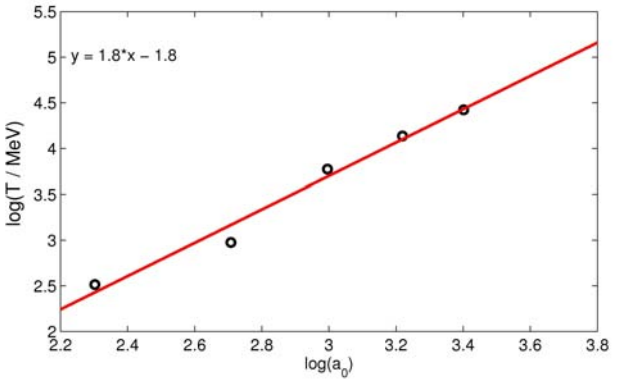

Figure 3. Log-log plot of the fast electron temperature against a_0 for a set of simulations with $n_e = 0.5n_c$ and r_L = 10μm. This shows a power law scaling of $a_0^{1.8}$ which is very close to the LED scaling of a_0^2.

Figure 3 shows the results of one check of the fast electron energy scaling with a_0. At low density where we expected the LED regime to apply we found a scaling of $a_0^{1.8}$ which is very close to the LED scaling of a_0^2. At high densities we observed a scaling of $a_0^{1.1}$ which is very close to the TPA scaling of a_0. At an intermediate density we observed a scaling of $a_0^{1.3\text{-}1.4}$, which lies between these two cases.

Overall we found that the 2D PIC simulations showed the existence of separate LED and TPA regimes with smooth transitions between them. In these distinct regimes, the gross properties are well predicted by the new analytic formulae that we have derived.

Conclusions

Two general ideas about how absorption occurs in near-critical plasma have existed for a number of years. In this body of work we have critically examined both ideas and derived new analytic formulae to describe the gross properties that improve on the existing formulae. Our simulations show that both ideas, Leading Edge Depletion and Transverse Ponderomotive Acceleration, can exist as distinct regimes and in these regimes the analytic formulae provide good predictions in comparison to the simulation results.

Acknowledgements

The authors are grateful for the use of computing resources provided by the Science and Technology Council's e-Science facility. The authors would also like to thank T.Arber, C.Brady, and the rest of the EPOCH team for their support.

References

1. C.Decker et al., Phys.Plasmas, **3**, 2047 (1996)
2. S.V.Bulanov et al., Phys.Scr., **47**, 209 (1992)
3. A.Macchi et al., Plasma Phys.Control.Fusion, **51**, 024005 (2009)
4. A.B.Borisov et al., Phys.Rev.A., **45**, 5830 (1992)

Modelling Spitzer transport in laser produced plasmas by direct Vlasov methods with a BGK collision operator

Contact *Nathan.Sircombe@awe.co.uk*

N J Sircombe

AWE plc. Aldermaston, Reading, Berkshire, RG7 4PR, UK

Centre for Fusion, Space and Astrophysics, Department of Physics, University of Warwick, Coventry CV4 7AL, UK

Central Laser Facility, STFC, Rutherford Appleton Laboratory, Chilton, Didcot, Oxfordshire, OX11 0QX, UK

T D Arber

Centre for Fusion, Space and Astrophysics, Department of Physics, University of Warwick, Coventry CV4 7AL, UK

Introduction

Collisional processes are of critical importance to short-pulse laser matter interaction. The absorption of incident laser energy is dominated by collisionless mechanisms[1,2,3]. However, the onward transport of the flux of fast moving, essentially collisionless, electrons and the resultant heating of the target is dependent on the response of the cold, resistive, background plasma.

Considerable progress has been made in modelling transport phenomena in both long and short pulse laser plasma interactions using an approach to the Vlasov-Fokker-Planck problem based on a decomposition of the electron distribution function into spherical harmonics, or a similar set of basis functions[4,5]. However, for modelling the laser-plasma interaction region directly a direct Vlasov solver is desirable: unfortunately, solving the VFP problem on the discrete phase space grid of a direct Vlasov solver is extremely demanding, computationally speaking[6].

Here we briefly outline a simple approach to including collisional physics in the direct Vlasov solver VALIS[7], based on the BGK (Bhatnagar, Gross and Krook) collision operator, which does not have the computational overheads associated with the VFP approach. We are able to demonstrate the efficacy of this approach in two key transport problems in laser plasma interaction: thermal conduction and electrical resistivity.

The Bhatnagar, Gross and Krook collision operator

Collisional effects form the right hand side of the Boltzmann equation but are absent from the Vlasov equation. They can be included in a Vlasov solver, such as VALIS, by the addition of an appropriate collison operator, so that for species *j*:

$$\frac{\partial f_j}{\partial t}+\frac{\mathbf{u}}{\gamma}\cdot\nabla_{\mathbf{x}} f_j+\frac{q_j}{m_j}\left(\mathbf{E}+\frac{\mathbf{u}}{\gamma}\times\mathbf{B}\right)\cdot\nabla_{\mathbf{u}} f_j=C_j\left(f_j\right) \quad (1)$$

where *C* represents the collision operator:

$$C_j\left(f_j\right)=\sum_k\left(\frac{\partial f_j}{\partial t}\right)_{C,k} \quad (2)$$

and $\left(\partial_t f_j\right)_{C,k}$ represents the change in f_k due to collisions with species *k*. Any collision operator should have the following characteristics: it must conserve mass, momentum and energy; it must have an *H*-theorem (that is to say it must asymptotically approach a unique equilibrium distribution in a homogenous plasma, the Maxwellian distribution); and it must maintain positive *f*. Here we consider and implementation of a simple BGK collision operator[8]:

$$\left(\frac{\partial f_j}{\partial t}\right)_{C,k}=-\nu_{jk}\left(f_j-F_j\right) \quad (3)$$

where υ_{jk} is the collision frequency for collisions between species *j* and *k* , F_j is the equilibrium distribution: Maxwell-Boltzmann in the non-relativistic limit and Maxwell-Jüttner in the relativistic case.

Following the treatment devised by Mannheimer et al.[9] we use the high and low energy collision frequencies from the NRL Plasma Formulary[10] analytically matched so that, for example, the electron-ion collision frequency becomes:

$$\nu_{ei}=\frac{6.43\times10^{-8}\ln\Lambda Z n_e}{\left(\frac{m_e}{m_i}T_i\right)^{3/2}+\frac{5.8}{7.7}E_{ne}{}^{3/2}} \quad (4)$$

where subscripts *e* and *i* denote electron and ion quantities respectively and E_{ne} represents the electron kinetic energy. The value of the Coulomb log is also taken from the NRL Plasma Formulary.

The BGK operator is treated implicitly so that, for electron-ion collisions only:

$$f_e^{n+1}-f_e^{n}=\nu_{ei}\Delta t\left(f_e^{n+1}-F_e\right) \quad (5)$$

giving:

$$f_e^{n+1}-f_e^{n}=\frac{\nu_{ei}\Delta t\left(f_e^{n}-F_e\right)}{\left(1+\nu_{ei}\Delta t\right)} \quad (6)$$

By taking velocity moments of Equation 6, it is clear that the BGK operator can be made to conserve energy, mass and momentum by a suitable choice of *F*. For the electron-ion collision term to have the correct conservation properties at each time-step we find the F_e which satisfies:

$$\int\left\{\frac{\nu_{ei}}{1+\Delta t\nu_{ei}}\left(\frac{u_e}{\gamma}\right)^m\left(f_e^{n}-F_e\right)\right\}du=0 \quad (7)$$

where *m* = 0, 1 or 2. Since the form of F_e is known we can simply calculate the density, drift speed and temperature of F_e iteratively. For the tests detailed here, we consider only the non-relativistic limit, fixing $\gamma = 1$, and do not impose conservation of momentum for any electron-ion collisions.

This implementation of the BGK approach has a number of desirable properties: it can be implemented an a fully implicit and conservative manner and implemented independently of the solution of Vlasov's equation; it can be applied to multi-species systems; the impact of collisions or changes to the underlying

physics can be easily assessed through changes to the calculation of the collision frequencies; and it does not rely on an expansion in the reciprocal of the Coulomb log.

This is potentially a practical way of including collisional effects in a direct Vlasov solver like VALIS. Inclusion of the full Landau form of the Fokker-Planck equation in an Eulerian Vlasov solver can be achieved[6], but at significant computational cost, which can make the application of such approaches impractical with the level of HPC resources currently available.

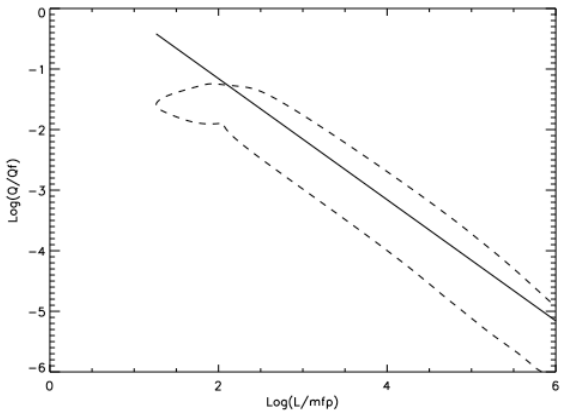

Figure 1. Ratio of calculated electron heat flux (Q) to the free streaming limit (Qf) as a function of scale-length over electron mean free path. The solid line is the Braginskii (Spitzer-Harm) predicted heat flux. The dashed line is the computed heat flux.

Thermal conductivity test

We initialise the system with a tanh profile for the electron temperature (from 400 eV down to 100eV), stationary ions (Z=4) and an electron number density of $2.97\text{x}10^{26}$ m^{-3} so that there are 100 particles per Debye sphere for the 100 eV electrons. The computed heat flux compared to Spitzer-Harm is plotted in Figure 1 after 1000 hot electron plasma periods. This shows heat flux limiting of ~0.1. The computed heat flux is multi-valued when plotted in this way, the lower section of the dashed curve corresponds to the hot side of the temperature profile and exhibits thermal flux limiting. The upper section corresponds to the cold side of the simulation and exceeds the Spitzer-Harm value, given by a solid line, due to the contribution from hot electrons from the higher temperature region. These results are in qualitative and quantitative agreement with previous simulations based on the full Fokker-Planck collision operator[11].

Plasma resistivity

Short-pulse laser plasma interaction at the target surface drives high energy 'hot' electrons into the body of the target. These electrons can generally be treated as collisionless, but they draw a return current of slow-moving collisional electrons[12], which are responsible in large part for heating the target as well as influencing the development of magnetic fields, which may in turn collimate the hot electron beam[13]. Therefore, it is important that any transport model intended for application to problems in short-pulse laser produced plasmas be able to reproduce well understood phenomena such as Spitzer resistivity.

We adopt a 1D1P system (one dimension in space and one in momentum) of mobile electrons and immobile protons 2nm in length and periodic in x, with initial electron and ion temperatures of 100eV and with a momentum extent equivalent to $\pm 20 v_{te}$, where v_{te} is the electron thermal velocity. A relatively coarse phase space resolution of 8 cells in x by 64 cells in u is utilised throughout. We choose an electron number density of 10^{29} m^{-3} and apply a fixed external electric field of between 10^7 and 10^9 Vm^{-1}, while disabling the code's Maxwell field solver.

The average current in x verses time can then be compared with the expected value:

$$J_{SH} = \frac{E}{\eta_{SH}} \tag{8}$$

where, considering only electron-ion collisions[14, 15]:

$$\eta_{SH} = \frac{\alpha_c m_e}{e^2 n_i \tau_{ei}} \tag{9}$$

and the collision time, is given as:

$$\tau_{ei} = 3\pi^{3/2}\varepsilon_0^2 \sqrt{m_e}\,\frac{(2k_B T_e)^{3/2}}{e^4 Z^2 n_i \ln\Lambda} \tag{10}$$

Here α_c is the classical transport coefficient calculated in Ref. 15 from the numerical solution of the Fokker-Planck equation and all quantities are given in SI units.

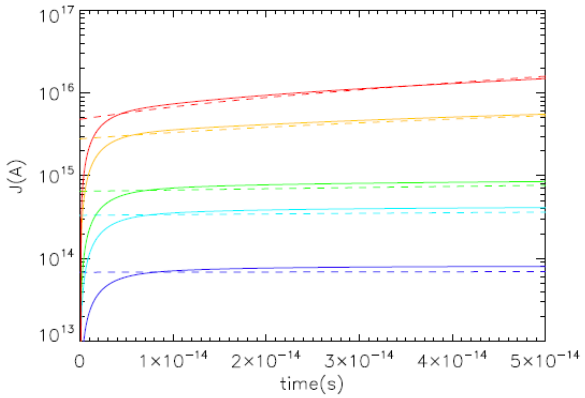

Figure 2. Comparison of Spitzer currents (dashed lines) with those calculated using VALIS with a BGK collision operator (solid lines) for external fields of: 10^7Vm^{-1} (blue); $5\text{x}10^7$Vm^{-1} (cyan); 10^8Vm^{-1} (green); $5\text{x}10^8$Vm^{-1} (yellow); and 10^9Vm^{-1} (red), for the case of electron-ion collisions only. The gradient of the lines is a result of Ohmic heating.

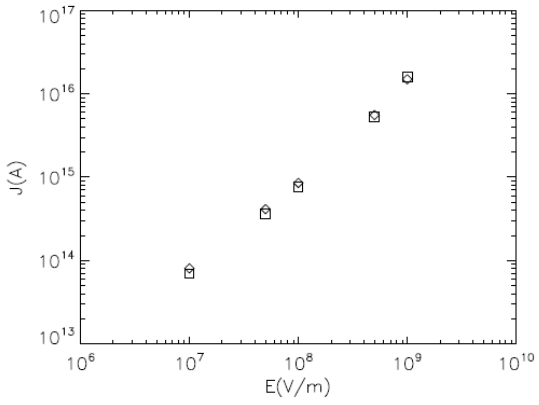

Figure 3. Comparison of Spitzer currents (squares) with those calculated using VALIS with a BGK collision operator (diamonds) after 50fs for a range of applied fields and including only electron-ion collisions.

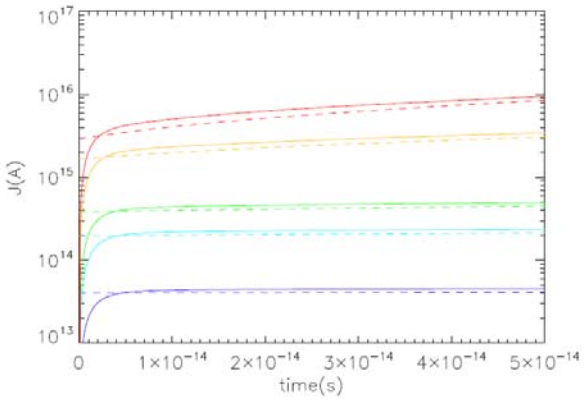

Figure 4. Comparison of Spitzer currents (dashed lines) with those calculated using VALIS with a BGK collision operator (solid lines) for external fields of: 10^7Vm^{-1} (blue); $5x10^7$Vm^{-1} (cyan); 10^8Vm^{-1} (green); $5x10^8$Vm^{-1} (yellow); and 10^9Vm^{-1} (red), for the case of both electron-electron and electron-ion collisions.

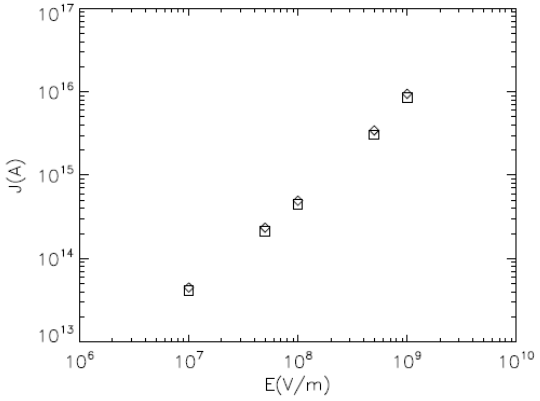

Figure 5. Comparison of Spitzer currents (squares) with those calculated using VALIS with a BGK collision operator (diamonds) after 50fs for a range of applied fields and including both electron-electron and electron-ion collisions.

Figures 2 and 3 summarise results for a range of external fields. VALIS, with the BGK collision operator is able to reproduce the expected Spitzer current across the range of fields. When the effect of electron-electron collisions (for which one must add an additional pre-factor of ~16/3π to equation 9) are included, the results are equally encouraging – as shown in Figures 4 and 5. Broadly similar results have been achieved at number densities of 10^{28} and 10^{29} m^{-3} over the range of fields. As one would expect, results in the low density, high field case display a higher drift velocity and demonstrate considerably more Ohmic heating, compared to the low field, high density case, where the deviation from the initial Maxwellian is much less pronounced, see Figure 6.

Conclusions

We have outlined a simple BGK collision operator for the Eulerian Vlasov solver VALIS. This implementation can be applied to multi-species systems including both inter and intra-species collisions and is formulated so that particle number, energy and momentum are conserved. Furthermore, the fully implicit implementation allows the method to be applied independently of the scheme used to solve Vlasov's equation[7,16].

Two simple 1D tests demonstrate the potential of this approach for modelling problems in laser-plasma interaction, making this approach a practical way of including collisional effects in a direct Vlasov solver like VALIS and allowing the self-consistent modelling of absorption and transport without the need to solve for the full Landau form of the Fokker-Planck equation. Ongoing work will extend this approach to higher dimensions, relativistic problems and realistic systems.

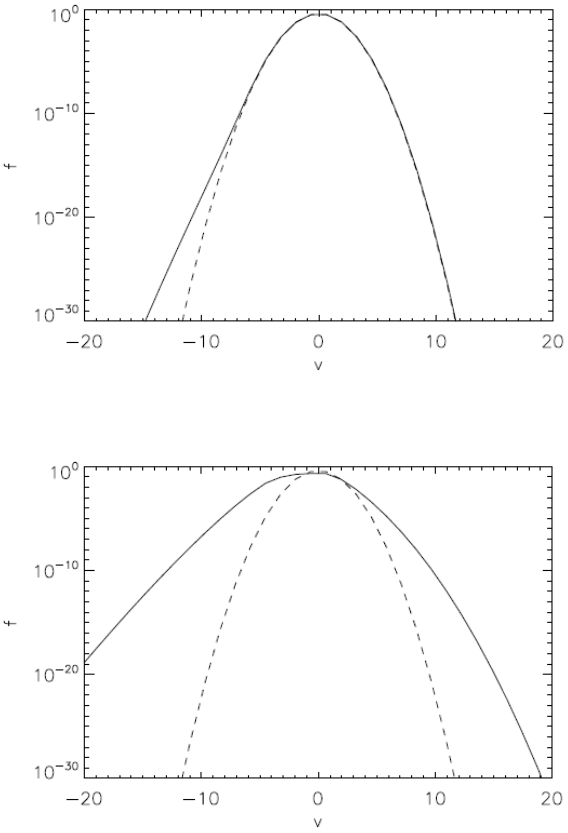

Figure 6. Initial (dashed line) and final, i.e. after 50fs, (solid line) velocity distribution functions for: an electron number density of 10^{30}m^{-3} and applied field of 10^7Vm^{-1} (top); an electron number density of 10^{30}m^{-3} and applied field of 10^7Vm^{-1} (bottom). The effect of Ohmic heating is clear in the low-density, high-field case.

Acknowledgements

The authors would like to thank Mark Sherlock for useful discussions on the plasma resistivity test problem.

References

1. S. C. Wilks *et al.*, *Phys. Rev. Lett.*, **69**, 1383 (1992)
2. F. Brunel, *Phys. Rev. Lett.*, **59**, 52, (1987)
3. P. Gibbon and A. R. Bell, *Phys. Rev. Lett.*, **68**, 1535, (1992)
4. A. R. Bell *et al.*, *Plasma Phys. Control. Fusion* **48**, R37 (2006)
5. R. J. Kingham and A. R. Bell, *J. Comp. Phys.* **194**, 1, (2004)
6. R. Duclous *et al. J. Comp. Phys.*, **228**, 5072, (2009)
7. N. J. Sircombe and T. D. Arber, *J. Comp. Phys.*, **228**, 4773 (2009)
8. P. L. Bhatnagar, E. P. Gross, E. P. and M. Krook, *Phys. Rev.* **94**, 511 (1954)

9. W. Manheimer *et al.*, *Phys. Plasmas*, **15**, 083103 (2008)

10. J. D. Huba, 2006 *NRL Plasma Formulary* (Washington D. C. : Naval Research Laboratory)

11. A. R. Bell, R. G. Evans and D. J. Nicholas, *Phys. Rev. Lett.*, **46**, 243 (1981)

12. A. R. Bell *et al.*, *Plasma Phys. Control. Fusion*, **39**, 653, (1997)

13. A. P. L. Robinson and M. Sherlock, *Phys. Plasmas*, **14**, 083105 (2007)

14. L. Spitzer, 1962, *Physics of fully ionised gases.*

15. E. M. Epperlein and M. G. Haines, *Phys. Fluids*, **29**, 1029, (1986)

16. T. D. Arber and R. G. L. Vann *J. Comp. Phys.*, **180**, 339, (2002)

Effect of channel profile evolution on laser-driven electron acceleration in plasma channels

Contact *raoul.trines@stfc.ac.uk*

R.M.G.M. Trines and P.A. Norreys

Central Laser Facility, Rutherford Appleton Laboratory
HSIC, Didcot, OX11 0QX

R.A. Fonseca and L.O. Silva

GoLP/Instituto de Plasmas e Fusão Nuclear
Instituto Superior Técnico, Lisbon, Portugal

C. Kamperidis, K. Krushelnick and Z. Najmudin

Imperial College, Blackett Laboratory
Prince Consort Road, London SW7 2BW, United Kingdom

Introduction

Plasma-based electron acceleration [1] holds the promise to deliver electrons at multi-GeV energies while requiring only a short acceleration distance. This was demonstrated most vividly when the energy of a 42 GeV electron beam was doubled in a 0.85 m long plasma in a beam-driven wakefield experiment [2]. While operating at lower energies, laser-driven wakefield acceleration has the advantage of producing electron bunches with an energy spread below 5% [3–5]. To increase the output energy of a plasma accelerator, one has to decrease the density of the background plasma and increase the acceleration length. In the case of laser-driven acceleration, this introduces the complication of laser pulse divergence. Without special measures, the length over which the laser pulse will stay spatially confined and capable of driving a decent wakefield is much shorter than the required acceleration length. An often used technique to overcome laser pulse divergence and increase the laser-plasma interaction length is pulse guiding by means of a preformed plasma channel. In such a channel, the plasma density is lowest along the channel's central axis, so the index of refraction is highest there and the laser pulse is guided as it would be in a glass fiber. In [4], a plasma channel was created by line-focusing a secondary laser pulse onto a gas jet; this channel was then used to guide the primary laser pulse. However, for longer acceleration lengths and lower plasma densities, plasma channels formed by hydrogen-filled capillary discharge waveguides [6, 7] are much more suitable. Using a 40 TW laser pulse guided by such a channel, electron bunches have been accelerated to up to 1 GeV with 5% energy spread [8].

Review of previous experimental results

Recently, laser wakefield acceleration in a hydrogen-filled capillary discharge waveguide was studied experimentally on the Astra Ti:sapphire laser at the Rutherford Appleton Laboratory [9]. During this experiment, plasma electron trapping and acceleration was observed. The accelerated electron bunches had a mean energy of up to 200 MeV and around 15 MeV spread. In addition, it was found that the probability of electron trapping was strongly dependent on the delay between the onset of the discharge current and the arrival of the laser pulse. Electron acceleration was only observed during a narrow delay interval, when the discharge current was already starting to switch off and laser energy transmission was past its peak. Interferometric and Raman spectroscopic measurements confirmed that electron trapping coincided with a decrease of both the degree to which the hydrogen was ionised and the depth of the plasma channel, i.e. with a general decrease in channel quality. No electrons were observed when the discharge current, laser energy transmission, channel depth and degree of hydrogen ionisation were at their peak, i.e. when the channel quality was optimal.

Simulation results

From these results, it is clear that electron injection in a plasma channel depends sensitively on the state of the plasma channel. In [9], it was suggested that the degree of ionisation may have a significant effect on electron trapping: electrons that are "born" during the passage of the laser will have a different velocity than free electrons that were already there, and may therefore be more eligible for trapping by the wakefield. However, other plasma parameters evolve simultaneously with the degree of ionisation, e.g. the overall plasma density and the transverse profile of the plasma channel. While it is not possible to isolate the effect of a change in each parameter in the experiments, it is certainly possible to do so in computer simulations. To investigate the influence of the degree of ionisation, as well as the background plasma density, channel profile and laser pulse intensity, on electron injection, we have performed a series of two-dimensional (2-D) numerical simulations using the particle-in-cell (PIC) code OSIRIS [10]. This code implements the full relativistic PIC algorithms, and also includes routines to model ionisation of neutral gases (H, He, Li, Ar). A series of simulations has been performed, in which the degree of ionisation (fully ionised, 1/3 neutral gas, 1/2 neutral gas), laser intensity ($0.8 < a_0 < 2.0$), plasma background density ($n_0 = (1 - 1.5) \times 10^{19}$ cm^{-3}) and channel profile ($n(r)/n_0 = 1 + a(r/r_0)^2$, where $0 < a < 0.033$) were varied. The results of these simulations can be summarised as follows:

- Increasing the laser intensity leads to a larger wakefield amplitude, causing the injection of more electrons which are subsequently accelerated to higher energies. These results are displayed in Figure 1.
- Increasing the plasma density by only 50% leads to a significant increase in both the number of trapped electrons and their energy after a fixed acceleration distance. If the acceleration could be continued for the entire dephasing length the final energy would be higher for lower densities, but in the experimental configuration used in [9] this is not realistic because of laser pulse depletion and finite channel length. These results are displayed in Figures 1 and 2.
- Decreasing the channel depth from 0.33 to 0.165 leads to only a moderate widening of the laser spot size without loss of guiding even for intensities as low as $a_0 = 0.8$. Removing the channel altogether leads to pulse divergence, lower wakefield amplitude and a decline in particle injection for the lowest intensities ($a_0 = 0.8$). For $a_0 > 1.0$, the laser pulse is sufficiently intense to guide itself via the process of relativistic self-focusing, and removing the channel has a much smaller impact. These results are displayed in Figures 2 and 3.
- Changing the fraction of neutral gas from 0 to 1/3 or 1/2 has a small effect on the transverse profile of the laser

pulse, but no significant effect on either the shape of the wakefield or the electron injection and acceleration processes. These results are displayed in Figure 4.

Discussion and conclusions

Based on the above simulation results, the experimental results of [9] can be explained by the following mechanism. When the discharge current is at its peak and the plasma channel is fully formed, the on-axis plasma density of $(0.5 - 1.0) \times 10^{19}$ cm^{-3} is slightly too low to trigger electron injection for the laser pulse intensity used ($a_0 \sim 0.6$). At later times, when the discharge current decreases, the plasma channel starts to "cave in", i.e. the on-axis density increases while the channel depth decreases. This can actually be concluded from Fig. 2 of [9], which shows an increase in the total density of available electrons (free and from re-ionisation), as well as a gradual flattening of the transverse density profile. Initially, the rising on-axis density leads to a sharp enhancement of electron injection, as well as the final electron energy. Following that, the flattening density profile leads to a loss of laser pulse confinement, meaning that the laser pulse is no longer able to efficiently generate a wakefield and electron injection stops altogether. We thus find that efficient electron injection and acceleration only happens for a rather special combination of circumstances, which explains the narrow window in which accelerated electrons were observed in the experiment.

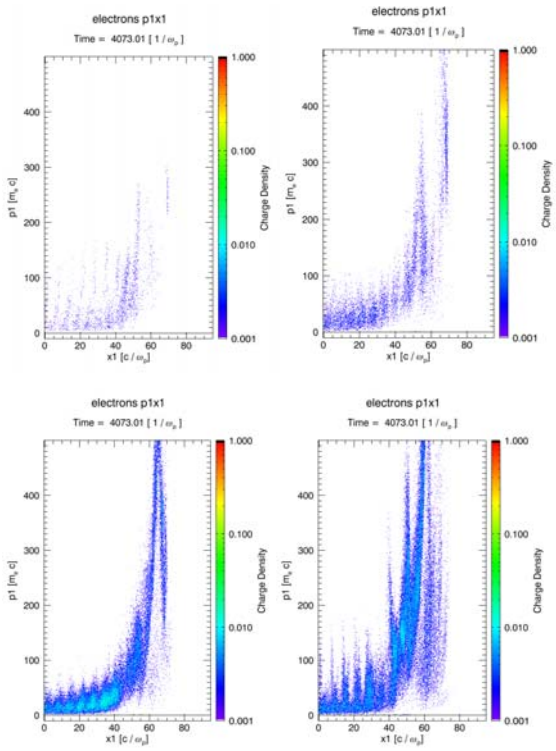

Figure 1. Electron trapping in a laser-driven wakefield, versus laser intensity. Laser amplitude a_0 is 1.19 (top left), 1.68 (top right), 2.0 (bottom left), 2.5 (bottom right), all other parameters equal. Laser spot diameter is 10 micron, wave length is 800 nm, ω_0/ω_p = 13.2, pulse duration is 50 fs. An increased laser intensity leads to enhanced electron trapping and acceleration.

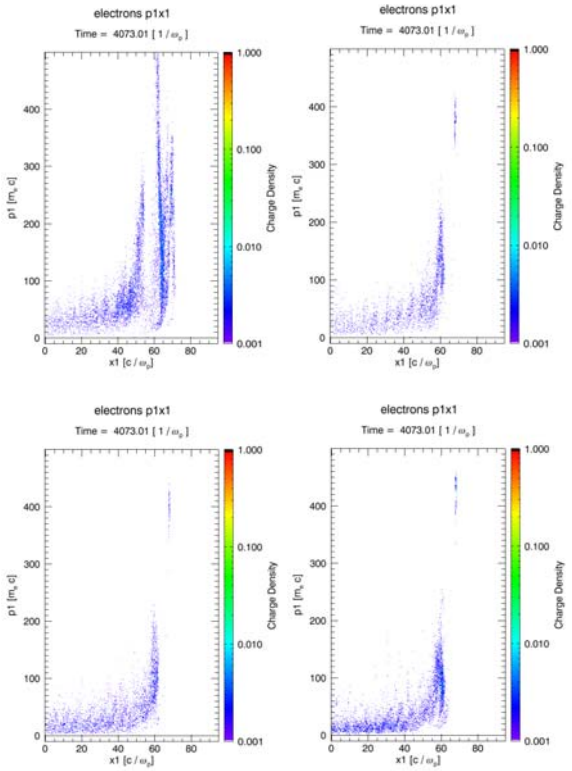

Figure 2. Top left: electron trapping for the same parameters as the top right frame of figure 1, except that ω_0/ω_p = 10.56, i.e. higher plasma density, leading to enhanced trapping and acceleration. Other frames: electron trapping versus channel depth for a_0 = 1.19 and ω_0/ω_p = 10.56. Channel depth is 0.33 (top right), 0.165 (bottom left) or 0 (bottom right). Reducing the channel depth leads to a decrease in electron energy, but self-focusing ensures that some electrons are trapped and accelerated even in the absence of a channel.

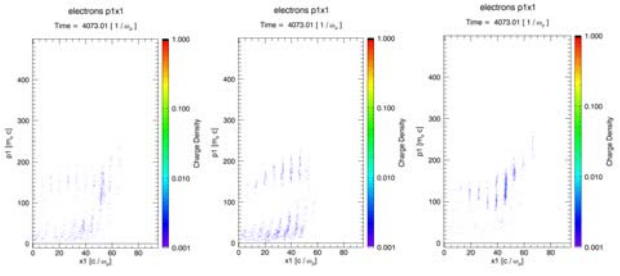

Figure 3. Electron trapping versus channel depth, for a_0 = 0.8. Removal of the channel inhibits wave breaking of the wakefield, leading to trapping of electron bunches at every wakefield period rather than a single bunch directly behind the laser pulse. This also has a detrimental effect on the energy spread.

In a separate simulation using a fully ionised plasma with a rather high temperature of 10 keV [11], it was found that the propagation mode of the laser pulse was different from propagation in a cold plasma, with the pulse in the cold plasma having two side lobes containing a significant fraction of the energy, while the pulse in the hot plasma had all its energy confined to one central lobe. Also, enhanced electron trapping was observed for the hot plasma. It was then suggested that re-ionisation of a partially recombined plasma by a passing laser pulse would lead to a fraction of electrons having a much higher temperature than the previously present free electrons, which would once again lead to better laser pulse confinement and enhanced electron trapping. However, while the simulations using a mixture of plasma and neutral gas did show a slight change to the transverse pulse profile on several occasions, this was not expressed in either a significantly higher electron

temperature or enhanced electron trapping. We therefore conclude that the enhanced electron trapping observed in the hot plasma entirely results from the artificially high plasma temperature. Indeed, it is well-known that wave breaking in warm plasma happens at a lower field amplitude than in cold plasma [12], while a small fraction of "thermal" electrons in a cold bulk plasma will still considerably lower the field threshold for electron trapping even if the wave itself does not break [13]. Combining Akhiezer and Polovin's equations for cold, relativistic plasma waves [14] and Ruth and Chao's Hamiltonian approach to quasi-static electron dynamics [13], we find the following expression for the wakefield amplitude necessary to trap an electron with initial forward speed v_t:

$$E_t \approx E_{wb}\left[1-(\gamma_\varphi v_t/2)^{1/2}+(\gamma_\varphi v_t/4)\right], E_{wb} = \sqrt{2(\gamma_\varphi - 1)}$$

Here, E_{wb} denotes the cold, relativistic wave-breaking field [14]. For γ_φ = 18 and "thermal" electron energies of 1, 10, 100 and 1000 eV, we find that Et/E_{wb} equals 0.87, 0.79, 0.66 and 0.53, respectively. This confirms that one can enhance electron trapping by increasing the plasma density and/or temperature, while changing the degree of ionisation does not really make an impact because the effect of that parameter on either density or temperature is simply too limited.

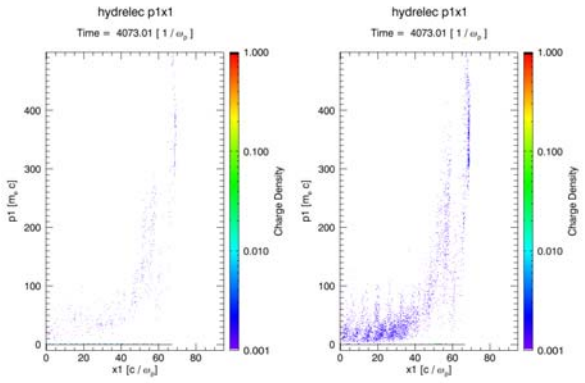

Figure 4. Energy spectrum of plasma electrons produced by ionisation processes in a partially ionized plasma: neutral fraction is 1/3 (left) or 1/2 (right). Other parameters are similar to the simulation depicted in the top right corner of Figure 1. Naturally the absolute number of electrons produced by ionisation increases with the fraction of neutrals, but their relative energy spectrum does not change much with the fraction of neutrals. The fraction of neutrals did not appear to produce qualitative changes in the energy spectrum of pre-existing electrons either.

Acknowledgements

This work was supported by the STFC Accelerator Science and Technology Centre and by FCT (Portugal) through grant PTDC/FIS/66823/2006. We would like to thank the OSIRIS consortium for the use of OSIRIS. Simulations were performed on the Scarf-Lexicon Cluster at the STFC Rutherford Appleton Laboratory.

References

1. T. Tajima and J.M. Dawson, Phys. Rev. Lett. **43**, 267 (1979).
2. I. Blumenfeld et al., Nature **445**, 741 (2007).
3. S.P.D. Mangles et al., Nature **431**, 535 (2004).
4. C.G.R. Geddes et al., Nature **431**, 538 (2004).
5. J. Faure et al., Nature **431**, 541 (2004).
6. D.J. Spence et al., Phys. Rev. E **63**, 015401 (2000).
7. A. Butler et al., Phys. Rev. Lett. **89**, 185003 (2002).
8. W.P. Leemans et al., Nature Phys. **2**, 696 (2006).
9. T.P. Rowlands-Rees et al., Phys. Rev. Lett. **100**, 105005 (2008).
10. R.A. Fonseca, L.O. Silva, R.G. Hemker, et al., Lect. Not. Comp. Sci. **2331**, 342 (2002).
11. C. Kamperidis, private communication.
12. R. M. G. M. Trines and P. A. Norreys, Phys. Plasmas **13**, 123102 (2006).
13. R. D. Ruth and A. W. Chao, AIP Conf. Proc. **91**, 94 (1982).
14. A. I. Akhiezer and R. V. Polovin, Zh. Exp. Teor. Fiz. **30**, 915 (1956) [Sov. Phys. JETP **3**, 696 (1956)].

A Vlasov-Fokker-Planck Code For Shock Ignition

Contact *m.tzoufras1@physics.ox.ac.uk*

M. Tzoufras

Clarendon Laboratory, University of Oxford, Parks Road, Oxford UK OX1 3PU

A. R. Bell

Clarendon Laboratory, University of Oxford, Parks Road, Oxford UK OX1 3PU

A 2D3P parallel object-oriented Vlasov-Fokker-Planck code that relies on the expansion of the electron distribution function to spherical harmonics has been developed, in order to study non-local electron transport for Shock Ignition. The code makes use of a rigorous formalism for the collisions between electrons, which derives from the Rosenbluth potentials and conserves energy and number. This code makes it possible to accurately model the kinetic as well as the hydrodynamic behaviour of the plasma and is particularly efficient for collisional plasmas. For Shock Ignition the electron temperatures range from more than 100keV to 10eV while densities range from less than critical to greater than solid. Shock Ignition is therefore an excellent candidate for this VFP code, because the target is sufficiently collisional to allow for extremely efficient modelling.

Introduction

The ability of hot electrons to transfer energy over large distances arises from the most fundamental properties of ionized matter and leads to complex and unpredictable phenomena. Understanding and controlling non-local electron transport is crucial for Shock Ignition [1-2], which aims to increase the energy gain for Inertial Confinement Fusion (ICF) [3] without major modifications to conventional ICF designs.

In Shock Ignition, hot electrons generated near the critical surface, due to a spike in the drive laser pulse, need to distribute the energy around the compressed pellet so as to launch a spherically convergent shock. The transport of this large population of hot electrons through and around the dense plasma is associated with the generation of strong electromagnetic fields, which in turn are determined by the plasma conductivity. In this regime the Spitzer conductivity does not apply and the correct kinetic description of the total electron distribution must be considered.

One can describe the evolution of the electron distribution function with the Vlasov-Fokker-Planck equation thereby retaining the kinetic treatment of the entire electron population:

$$\frac{\partial}{\partial t} f + \mathbf{u}\cdot\frac{\partial}{\partial \mathbf{r}} f + q(\mathbf{E}+\frac{\mathbf{u}}{c}\times\mathbf{B})\cdot\frac{\partial}{\partial \mathbf{p}} f = \left(\frac{\delta f}{\delta t}\right)_{ei} + \left(\frac{\delta f}{\delta t}\right)_{ee}$$

where $f(\mathbf{p},\mathbf{r},t)$ is the electron distribution function and the terms $(\delta f/\delta t)_{ei}$ and $(\delta f/\delta t)_{ee}$ describe the contributions of electron-ion and electron-electron collisions respectively. The Fokker-Planck (FP) equation resembles a Taylor expansion for small-angle deflections in velocity space and assumes linear addition of the effects of all particles within a Debye length (λ_D). Because of this cutoff and the neglect of high-order terms the FP description implies a large number of particles (N_D) within a Debye sphere and fails for very high densities and very low temperatures. There is, nevertheless, a large volume of plasma between the laser-plasma interface and the ultra-high density region, which is described well by the FP equation. In the plasma corona there are more than 100,000 electrons per Debye sphere, while in the high-density plasma their number drops to 10-100, e.g. for T=300eV and n=10^{23}/cc N_D~30.

The main difficulty in solving the Vlasov equation numerically comes about from the 6D nature of the electron distribution function, with three dimensions used for real space and three dimensions for phasespace, so that even if a modest number of cells is used per dimension the grid ends up being prohibitively large. Instead, one can expand the distribution function in phasespace to spherical harmonics and express it using the complex amplitudes of the expansion and a 1D grid for the magnitude of momentum [4].

$$f(\mathbf{p},\mathbf{r},t) = \sum_{l=0}^{\infty}\sum_{m=-l}^{l} f_l^m(|\mathbf{p}|,\mathbf{r},t) P_l^{|m|}(\cos\vartheta) e^{im\varphi}$$

$$0 \le \vartheta = \arccos(p_x/|\mathbf{p}|) < \pi, \quad 0 \le \varphi = \arctan_2(p_z,p_y) + \pi < 2\pi$$

where $f_l^{-m} = [f_l^m]^*$ the amplitudes of the expansion and P_l^m the associated Legendre functions. The spherical harmonics are characterized by two indices l,m, where large l,m correspond to highly directional/anisotropic harmonics (Fig. 1).

The main advantage of this approach is that angular scattering due to collisions between electrons and ions tends to isotropize the distribution function by rapidly damping the high-order harmonics. It is therefore possible to capture the physics using only few terms in the expansion, and reduce the problem size, compared to a regular Vlasov code, by a factor in excess of 1,000. Other advantages of this expansion are that it makes it easier to stretch the phasespace, that it allows one to resolve the magnitude of momentum much more finely than the angle, and that it makes it easier to include collisions between electrons. On the other hand, its main vulnerability, the singularity at the origin p = 0, can be effectively addressed in the numerical scheme.

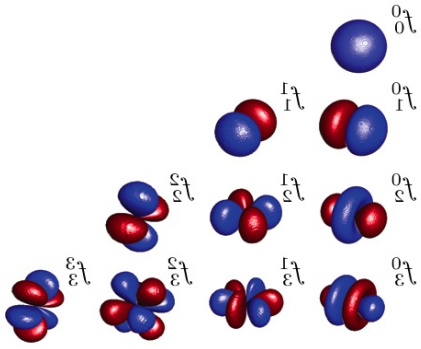

Figure 1: The first ten spherical harmonics

Numerical Grid

The expansion to spherical harmonics results in an irregular grid in phasespace (Fig. 2a), with the smallest cell at the origin. Numerical stability—assuming an explicit scheme—requires that a sufficiently small time-step and/or a high-order integration method be used to resolve the highest order harmonic at the smallest cell (e.g. Fig. 2b-2c). Alternatively one can restrict the number of harmonics resolved for low-momentum cells (Fig. 2d). This makes the code stable even for relatively large time-steps, but can lead to some artificial noise. At low-momentum cells, even a very small amount of collisionality damps this artificial noise immediately.

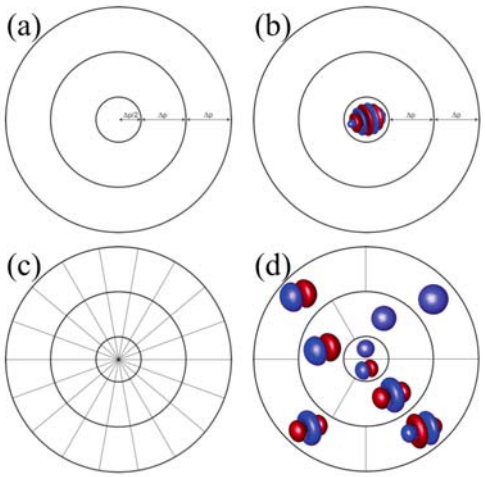

Figure 2: (a) First three |p|-cells, (b)-(c) keeping all f_l^m for all |p|-cells, (d) keeping only low f_l^m for low |p|-cells.

Parallelization is achieved by decomposing the computational domain in real space, which is represented in a Cartesian grid.

2D3P Vlasov code

The following normalizations are adopted to model the Vlasov-Maxwell set of equations:

$$t \to \omega_p t \quad r \to k_p r \quad p \to p/(m_e c) \quad n \to n/n_p \quad q_e \to -1$$

$$f \to c^3 f/n_p \quad \{E \text{ or } B\} \to e\{E \text{ or } B\}/(m_e c \omega_p)$$

where the subscript "p" indicates the maximum initial plasma density. The full 3D electromagnetic fields along with spatial advection in 2D (x,y) have been implemented in an explicit scheme following Ref. [4]. The object-oriented design allows for interchangeability of numerical operators, which has made it possible to incorporate a number of numerical methods and compare their performance in terms of speed, accuracy and stability. The code has been tested for standard plasma physics problems, e.g. the (collisionless) two-stream instability and (collisionless) plasma expansion. The evolution of these phenomena is modeled well up to a point, after which more harmonics have to be added to accurately describe the physics. Once collisions are added the need to continually add high order harmonics disappears. For collisionless plasmas the applicability of the expansion to spherical harmonics is limited to cases with slow spatial variation and weak electric field.

A laser source is mocked by substituting part of the distribution function with a new distribution function with a temperature determined by the characteristics of the laser. The code can generate output that includes the fields, the moments of the distribution function and allows for the conversion of the entire electron distribution function to a Cartesian grid so that it can be displayed using standard visualization software. Periodic and reflecting boundaries have been implemented.

Electron-ion collisions

Collisions involve predominantly low-energy particles. We assume that relativistic effects can be ignored in the collision operators and use the standard non-relativistic Fokker-Planck formalism in Ref. [5]. The expression for the evolution of the amplitude of each harmonic f_l^m due to collisions between electrons and ions becomes:

$$\left(\frac{\delta f_l^m}{\delta t}\right)_{ei} = -\frac{l(l+1)}{2}\nu_{ei} f_l^m$$

where $\nu_{ei} = n_i Y_{ei}/\upsilon^3$ with $Y = 4\pi\left(ZZ'e^2\right)^2 \ln\Lambda/m^2$ and $Y_{ei} \equiv Y(Z'=1, m=m_e)$. Angular scattering leads to damping of each f_l^m with a rate proportional to $l(l+1)/2$. That is, the more anisotropic/directional a harmonic is the faster it decays, as angular scattering tends to smooth out the shape of the distribution function. This makes it possible to truncate the expansion keeping only few harmonics for collisional plasmas. Additionally, because the collision-time scales with the cube of the velocity, even fewer terms are needed in the low-momentum cells. This relaxes the restrictions on the time-step significantly. To derive a characteristic time for angular scattering we use the expression for the RMS velocity $m\langle\upsilon^2\rangle = 3kT$ to obtain $\tau_e = 3.44\times10^5 \times \frac{(T_e[eV])^{3/2}}{n[cm^{-3}]\times\ln\Lambda}\sec$. The Coulomb Logarithm in the code is calculated using the expressions in the NRL Plasma Formulary.

Electron-electron collisions

The Fokker-Planck equation for any two species can be written as in Ref. [5]:

$$\frac{1}{Y}\left(\frac{\delta f}{\delta t}\right) = 4\pi\frac{m}{M}Ff + \left(\frac{M-m}{M+m}\right)\nabla \mathrm{H}(F)\cdot\nabla f + \frac{\nabla\nabla \mathrm{G}(F):\nabla\nabla f}{2}$$

where F is the distribution function and M is the mass of the scatterer and H,G (the Rosenbluth potentials [6]) are integral functions for F. This equation can be linearized by assuming that the anisotropic part of the distributions F, f is a perturbation to the isotropic part: $F = F_0^0 + F_a, f = f_0^0 + f_a$. This yields a nonlinear equation for the isotropic part and a linear equation for the anisotropic part of the distribution. The full derivation of the expressions for any two species will be presented elsewhere.

For collisions between electrons, where $F \equiv f$, the nonlinear equation for the isotropic part of the distribution can be written:

$$\left(\frac{\delta f_0^0}{\delta t}\right)_{ee} = \frac{4\pi Y_{ee}}{3}\frac{1}{\upsilon^2}\frac{\partial}{\partial\upsilon}\left[\frac{1}{\upsilon}\frac{\partial G}{\partial\upsilon}\right]$$

$$G = f_0^0\int_0^{\upsilon} f_0^0 u^4 du + \upsilon^3 f_0^0\int_{\upsilon}^{\infty} f_0^0 u du - 3\int_{\upsilon}^{\infty} f_0^0 u du\int_0^{\upsilon} f_0^0 u^2 du$$

This formulation allows developing a numerical scheme that conserves energy and number of electrons. For velocities on the order of $\sqrt{kT/m}$ or larger any regular expression for the integrals above suffices. For $\upsilon << \sqrt{kT/m}$ the second and third terms in the equation for G vanish up to $O(\upsilon^5)$, and the Taylor-expanded form of f_0^0 must be used. This ensures that f_0^0 relaxes to a Maxwellian. An explicit scheme can be used for this nonlinear equation. The time-step for this integration can be a fraction of the time-step for the Vlasov part of the code, but since it involves only one harmonic f_0^0 and only a few simple calculations it does not affect the overall performance of the code.

To simplify the expression for high order collisions we define the integrals:

$$I_j(f_l^m) = \frac{4\pi}{\upsilon^j}\int_0^{\upsilon} f_l^m u^{j+2} du \quad J_j(f_l^m) = \frac{4\pi}{\upsilon^j}\int_{\upsilon}^{\infty} f_l^m u^{j+2} du$$

The equation for high-order harmonics becomes:

$$\frac{1}{Y_{ee}}\left(\frac{\delta f_l^m}{\delta t}\right)_{ee} = 8\pi f_0^0 f_l^m + \frac{I_2(f_0^0) + J_{-1}(f_0^0)}{3\upsilon}\frac{\partial^2 f_l^m}{\partial\upsilon^2} +$$

$$\frac{-I_2(f_0^0) + 2J_{-1}(f_0^0) + 3I_0(f_0^0)}{3\upsilon^2}\left(\frac{\partial f_l^m}{\partial\upsilon} - \frac{l(l+1)}{2}\frac{f_l^m}{\upsilon}\right) +$$

$$\frac{1}{2\upsilon}\frac{\partial^2 f_0^0}{\partial\upsilon^2}\left[C_1 I_{l+2}(f_l^m) + C_1 J_{-1-l}(f_l^m) + C_2 I_l(f_l^m) + C_2 J_{1-l}(f_l^m)\right] +$$

$$\frac{1}{\upsilon^2}\frac{\partial f_0^0}{\partial\upsilon}\left[C_3 I_{l+2}(f_l^m) + C_4 J_{-1-l}(f_l^m) + C_5 I_l(f_l^m) + C_6 J_{1-l}(f_l^m)\right]$$

This is a linear equation for f_l^m with the constants $C_i(l)$ given in the Appendix. $f_0^0(t+\Delta t)$, which has been calculated from the nonlinear equation above, can be used to integrate implicitly

for f_l^m. The first two lines in this equation yield the scattering of f_l^m due to the Rosenbluth potentials calculated from f_0^0. This includes an "angular scattering" term $\propto[l(l+1)/2]f_l^m/v^3$. The last two lines can be seen as the effect that f_0^0 has on the Rosenbluth potentials calculated from f_l^m. We note that while the "scattering term" is of order $O(l^2)$, all other terms are of order $O(1)$ and they may be neglected for $l>>1$.

Benchmark

In order to study Shock Ignition the collision modules have been attached to the Vlasov code above. To test their accuracy we calculated the Spitzer heat conduction:

$$\frac{\mathbf{q}}{nm_e v_t^3} = -\left(\frac{320}{3\pi}\delta_T\varepsilon\right)\frac{v_t}{\langle \nu_{ei}\rangle}\frac{\nabla T}{T}$$

where δ_T,ε are given in Ref. [7] and $\langle \nu_{ei}\rangle = Z/(\omega_p\tau_e)$. This includes the effects of both electron-ion and electron-electron collisions. We simulated a plasma with density n=10^{23}/cc and a sinusoidal temperature profile with T_{min} =300eV and T_{max}=323eV. Spitzer heat conduction was recovered with error less than 0.2% throughout the simulation box (with length 1000 mean free paths). If the Rosenbluth potentials calculated from f_l^m are neglected the error increases to 4%.

Appendix

Coefficients in the linearized Fokker-Planck:

$$C_1=\frac{(l+1)(l+2)}{(2l+1)(2l+3)};\quad C_2=-\frac{(l-1)l}{(2l+1)(2l-1)};\quad C_3=\frac{-l(l+1)/2-(l+1)}{(2l+1)(2l+3)};$$

$$C_4=\frac{-l(l+1)/2+(l+2)}{(2l+1)(2l+3)};\quad C_5=\frac{l(l+1)/2+(l-1)}{(2l+1)(2l-1)};\quad C_6=\frac{l(l+1)/2-l}{(2l+1)(2l-1)}$$

References

[1] R. Betti, C. D. Zhou, K. S. Anderson, L. J Perkins, W. Theobald and A. A. Solodov, *Phys. Rev. Lett.* **98**, 155001 (2007) "Shock Ignition of Thermonuclear Fuel with High Areal Density."

[2] X. Ribeyre, G. Shurtz, M. Lafon, S. Galera and S. Weber, *Plasma Phys. Control. Fusion* **51**, 015103 (2009) "Shock ignition: an alternative scheme for HiPER."

[3] J. D. Lindl, *Inertial Confinement Fusion* (Springer-Verlag, New York 1998.)

[4] A. R. Bell, A. P. L. Robinson, M. Sherlock, R. J. Kingham and W. Rozmus, *Plasma Phys. Control. Fusion* **48**, R37-R57 (2006) "Fast electron transport in laser-produced plasmas and the KALOS code for solution of the Vlasov-Fokker-Planck equation."

[5] I. P. Shkarofsky, T. W. Johnston and M. P. Bachynski, *The Particle Kinetics of Plasmas* (Addison-Wesley Publishing Company, Inc. 1966.)

[6] Marshall N. Rosenbluth, William M. MacDonald, and David L. Judd, *Phys. Rev.* **107**, 1-6 (1957) "Fokker-Planck Equation for an Inverse-Square Force."

[7] Lyman Spitzer, Jr., and Richard Härm, *Phys. Rev.* **89**, 977-981 (1953) "Transport Phenomena in a Completely Ionized Gas."

Multi-component effects on the x-ray scattering signal from warm dense matter

Contact *K.Wuensch@Warwick.ac.uk*

K. Wünsch, J. Vorberger and D.O. Gericke

Centre for Fusion, Space and Astrophysics,
Department of Physics, University of Warwick,
Coventry CV4 7AL, UK

G. Gregori

Clarendon Laboratory, University of Oxford,
Parks Road, Oxford OX1 3PU, UK

Introduction

High-power and high-energy laser sciences open the way to create and study warm dense matter (WDM) in a controlled laboratory environment. Characterized by near solid density and temperature of a few electronvolts, WDM contains the states between condensed matter physics and the ideal plasma regime. At these conditions, one has to describes matter in a highly correlated state that is also governed by electron degeneracy and bound states. Therefore, WDM still poses many challenges for both theoretical and experimental studies. From the theoretical point of view, the occurrence of strongly coupled ions prohibits the use of well-know perturbation methods developed for ideal plasmas whereas the degenerate electrons require a fully quantum-mechanical description.

WDM research is also driven by the aim to achieve energy by means of inertial confinement fusion [1, 2], where it occurs in the converters and as a transient state in the core. In addition, the properties of WDM are required to develop a better understanding of astrophysical objects as it naturally occurs in the interior of giant planets and in the outer layers of old stars such as white and brown dwarfs or neutron stars [3,4]. During the last decade WDM can be created in a rapidly increasing number of powerful laser facilities worldwide. First experiments on different materials, e.g., Be, Li, CH and LiH [5,6,7,8], have demonstrated that high energy density matter has very interesting properties.

Besides generation, the diagnostics of WDM poses a severe challenge. Due to the high particle density, energetic particle beams or x-rays are required to penetrate the system. The scattering of x-rays has been shown to reflect the microscopic structure as well as being able to determine the basic plasma parameters like electron density, ion charge and temperature [9]. The application of x-ray scattering as a diagnostic method however relies on theoretical models for the structure of the material under investigation since the plasma parameters are deduces as a fitting parameter that allow to match the scattered signal with the theoretical description.

For composite materials like LiH or CH multiple components must be included in the description of WDM. The mutual interplay between the different highly correlated ions constitutes additional problems for a consistent theoretical description of the x-ray scattering signal. In this contribution, we present a theoretical model to describe the elastic Rayleigh peak in a multi-component system. The structural information needed are obtained by a quasi-classical approach that uses the hypernetted chain (HNC) equations which can be extended to treat multiple ion species [11,12]. For classical ion-systems, HNC has been proven to describe strong coupling effects very well [10]. The degenerate electrons in WDM can only be incorporated in an approximate way: here, we use a linearly screened Coulomb potential for the ionic interactions which is screened by a Thomas-Fermi like screening length. Nevertheless, this approach provides an efficient method to analyse experimental data. In contrast, full quantum simulations such as density function molecular dynamics (DFT-MD) [12] are capable to fully describe a complex WDM system, i.e., strongly coupled ions combined with degenerate electrons. However, such a treatment requires a high numerical effort and its applicability as an experimental analysis tool is thus very limited. We mainly use it to benchmark the classical HNC calculations and to determine charge states and inter-ionic potentials [12].

Theoretical description of the scattering signal

The spectrum of the scattered radiation per solid angle dΩ and per frequency interval dω is directly proportional to the microscopic structure of the electrons. In a many particle system this is expressed by the total dynamic electronic structure factor

$$P_S(k,\omega)d\omega\, d\Omega \propto S_{ee}^{tot}(k,\omega). \quad (1)$$

Here, k and ω denote the momentum and the energy change of the scattered photon, respectively. The structure factor for partially ionised matter, which is the Fourier transform of the correlation function of electron density fluctuations, can be decomposed with respect to electron fluctuations due to the ions and the free gas response (neglecting core excitations) [13,14]

$$S_{ee}(k,\omega) = \left|f(k)+q(k)\right|^2 S_{ii}(k,\omega) + Z S_{ee}^{0}(k,\omega). \quad (2)$$

The first contribution dominates the low frequency domain of the x-ray Thomson scattering signal and is strongly modulated by the strongly correlated ions. Here, electrons bound to the nucleus, characterised by the atomic/ionic form factor f(k), and the electrons in the screening cloud, described by q(k), contribute to the scattering of the probe beam. The second part of Eq. (2) describes the scattering due to the free electrons where Z denotes the number of free electrons per atom. This part describes the large frequency regime where the Compton shifted electron features as well as collective excitations (plasmons) can be observed. Effects of internal excitations and ionisation induced by the probe beam can be neglected in the low-Z materials considered here.

For the theoretical description of x-ray Thomson scattering, the microscopic structure expressed by the different structure factors has to be determined. The large frequency electron feature corresponds to the electron-electron structure factor of free electrons that is directly related to the correlation function of the density fluctuation by the fluctuation dissipation theorem [15]. In WDM, the electrons are degenerate and mostly weakly coupled. Thus, the random phase approximation (RPA) is an accurate description which can be improved by inclusion of electron-ion collisions (see e.g. Ref. [16]).

The ion feature, that describes the electrons co-moving with the ions, is directly related to the ion-ion structure factor describing the spatial arrangement and the thermal motions of the ions. Due to the finite bandwidth of the x-ray probe beam as well as the finite resolution of the detector, this quantity cannot be resolved in experiments with laser-driven sources. Thus, it is sufficient to use the frequency-integrated or static description $S_{ii}(k) = \int S_{ii}(k,\omega)d\omega$ for the ionic correlations. Here, the static structure factor is calculated using the HNC approach. As effective interaction potential between the ions, a Coulomb

potential linearly screened by the electrons is applied. This model yields similar results as *ab initio* simulations [12]. The atomic form factor of ions in plasmas can be approximated very well by the one for isolated atoms [17]. For light elements like beryllium where only 1s or 2s electrons occur, it is sufficient to use hydrogen-like wave function with an effective core charge [18]. The screening function q(k) that specifies the (free) valence electrons surrounding the ions, can be approximated within the linear response theory, that is by $q(k) = Z\kappa_e^2/(\kappa_e^2 + k^2)$, where κ_e is the inverse electron screening length [19].

Recent experiments were performed on systems with more than one ion species [7,8]. This raises the question how the mutual correlations within the ion system affect the scattering process. We generalised Eq. (2) for systems with an arbitrary number of ion species using a derivation similar to the original Chihara approach for single ion species which splits the electron density into bound and free contributions [13,14]. The result for the elastic ion feature W_R (k), that is the Rayleigh peak, can be summarised as

$$W_R^{\alpha\beta}(k) = \sum_{\alpha,\beta} \frac{\sqrt{n_\alpha n_\beta}}{n_i} (f_\alpha + q_\alpha)(f_\beta + q_\beta) S_{\alpha\beta}(k) \,. \quad (3)$$

Here, the summation runs over the different ion species α and β with the corresponding ion densities n_α. n_i denotes the total ion density in the system. Moreover, the partial ion-ion structure factors need now to be considered. The HNC approach, which can be applied to systems with multiple ion species [11], naturally describes the mutual correlations between the different ion species. Similarly, *ab initio* calculation like DFT-MD can be used for systems with more than one ion species. However, the already high computational demand strongly increases here with the number of species. The determination of the atomic or ionic form factors as well as the screening functions for the various ion species can be done in a similar fashion as for simple one-component systems.

Results and Discussion

Figure 1 presents the ionic structure as well as the weight of the Rayleigh peak for a dense CH plasma. At the temperature considered, the ionisation state of the carbon ions is Z = 2 whereas hydrogen is fully ionised. In the lower panel of the figure, the partial structure factors are shown. Under these plasma conditions, the higher charged carbon ions exhibit a more distinct structure than the protons or the cross term. In fact, the protons are only moderately coupled with a classical coupling parameter of Γ = 1.3. They can be nearly described as a uniform background as demonstrated by the almost constant structure factor that is typical for a weakly coupled system. However, strongly coupled ion species can imprint their structure on the other ion species. Moreover, the mutual correlations in the multi-component system lead to an additional screening due to the other species that is self-consistently included within the HNC equations. Note, that the partial structure factor S_{CH}(k) presents the typical characteristics of the cross terms where unity is not added in the definition [20] and negative values appear for small k (the long-range limit is zero). The total structure factor is however positive definite.

The upper panel of Fig. 1 shows the elastic ion feature (strength of the Rayleigh peak) for CH given by Eq. (3). The required form factor for carbon is taken for isolated double charged carbon [18]. Due to the fact that hydrogen is fully ionised, only the screening function and no atomic form factor has to be considered. This quantity is calculated in linear response as defined above (however, different screening clouds for carbon ions and protons are considered). The resulting weight of the Rayleigh peak is shown as a solid red line in Fig. 1. Furthermore, the different contributions related to the different

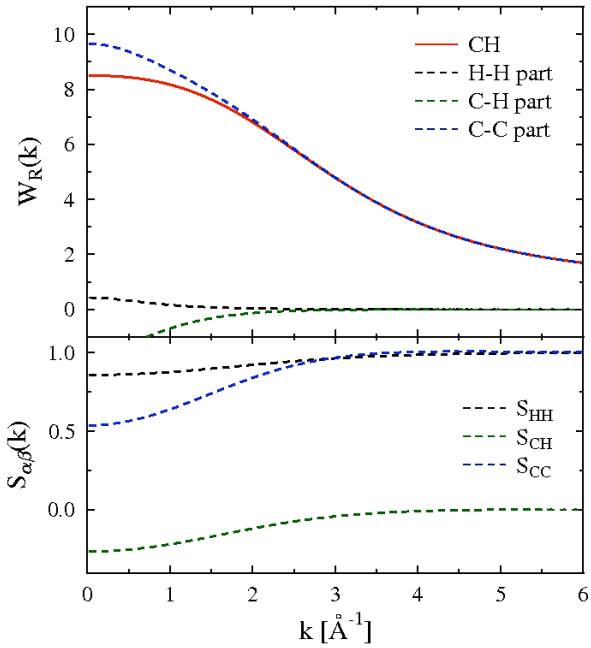

Fig. 1: The structure of a CH plasma with an ion density of $n_C = n_H = 5{\cdot}10^{22}$ cm^{-3}, a temperature of T = 8 eV and $Z_H = 1$ and $Z_C = 2$. The upper panel shows the weight of the Rayleigh peak (solid line) and its three contributions due to variations of carbon ions and protons (dashed lines). The lower panel shows the partial structure factors for CH.

combinations of C and H ions are plotted in the figure. This comparison makes it clearly visible that the elastic ion peak is mainly given by the scattering on the C^{2+} ions. For small k values the combination of all quantities are relevant whereas for larger distance, only the form factor of the carbon ions characterises the ion peak. Thus, forward scattering, which highlights the small k regime, is more sensitive to multi-component effects described here.

As a next example, we compare the strength of the elastic scattering for pure carbon, CH and a CH_2 with a constant carbon density to study the influence of the protons in the systems. In Fig. 2, the carbon structure factors are presented for

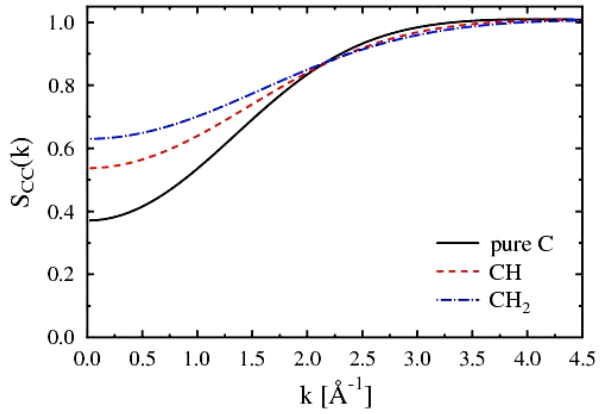

Fig. 2: Static carbon-carbon structure factors for warm dense carbon, CH and CH_2 calculated with the HNC method. The carbon density of $n_C = 5{\cdot}10^{22}$ cm^{-3}, the temperature of T = 8eV and a charge state of $Z_C = 2$ are fixed for all systems. For the calculation of CH and CH_2, fully ionised hydrogen, i.e. Z_H=1, with densities of $n_H = 5{\cdot}10^{22}$ cm^{-3} and $n_H = 10^{23}$ cm^{-3} is applied, respectively.

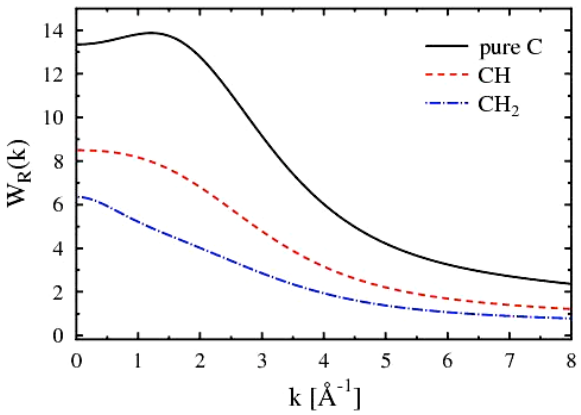

Fig. 3: Comparison of the weight of the Rayleigh peak for warm dense carbon, CH and CH_2. The plasma conditions are the same as in Fig. 2.

the different cases using one and two-component HNC with a screened Coulomb interactions, respectively. The pure carbon plasma shows the most pronounced structure. With the increase of proton density, the structure factor rises for small k values. This is due to the fact that the protons in the system contribute to further screening of the carbon-carbon interactions and, thus, the coupling decreases. Obviously, this effect becomes more significant with a higher proton density in the case of CH_2.

Fig. 3 shows the weight of the Rayleigh peak for the pure carbon, CH and CH_2 as in Fig. 2. The form factors for the carbon ions and the screening functions are calculated in the same manner as for CH described in Fig. 1. The weight of the Rayleigh peak for a pure carbon plasma simplifies to $W_R(k) = (f_C + q_C)^2 S_{CC}(k)$, whereas three contributions have to be added for the two systems of plastics. With the occurrence of protons in the system, the ion peak decreases nearly by a factor of two. This reflects the change in the partial structure factors due to the multi-component description. Furthermore, even though the weight of the Rayleigh peak is mainly dominated by the scattering on the carbon ions the fully multi-component description is necessary to get the correct statistical weight given by the densities of the elements considered. An increase of the proton density, like given with CH_2, leads to a further decrease of the elastic ion feature.

Conclusions

In this contribution, we investigate the effects of multiple ion species on the x-ray scattering process from warm dense matter. In particular, we discuss elastic scattering, that is, the weight of the Rayleigh peak. Based on partial structure factors from hypernetted chain solutions, a generalised approach of the theoretical model is applied to account for multi-component effects. We demonstrate that mutual correlations significantly influence the partial structure factors due to the fact that the ions with the highest charge imprint their structure on the other components. The weight of the Rayleigh peak that is directly related to the static structure factors is thus also sensitive to the interplay between the different correlated ions in the systems. These effects are especially pronounced in the case of forward scattering, i.e. for small k values. Furthermore, we demonstrate that the full multi-component description is also necessary for cases where x-ray scattering is dominated by one species. This effect is related to the differences in the statistical weight of the different contributions to the Rayleigh peak.

Acknowledgements

This work was supported by the EPRSC grants (EP/D062837, and EP/G007187/1) as well as the Science and Technology Facilities Council of the United Kingdom.

References

1. J.D. Lindl, *Inertial Confinement Fusion* (Springer, New York, 1998).
2. S.H. Glenzer *et al.*, Science **327**, 1228 (2010).
3. T. Guillot, Science **286**, 72 (1999).
4. B. Militzer, W.B. Hubbard, J. Vorberger, I. Tamblyn, and S.A. Bonev, Astro. Phys. J. Lett. **688**, L45 (208).
5. S.H. Glenzer *et al.*, Phys. Rev. Lett. **90**, 065002 (2007).
6. E. García Saiz *et al.*, Nature Phys. **4**, 940 (2008).
7. B. Barbrel *et al.*, Phys. Rev. Lett. **102**, 165004 (2009).
8. A.L. Kritcher *et al.*, Phys. Rev. Lett. **103**, 245004 (2009).
9. G. Gregori, S.H. Glenzer, W. Rozmus, R.W. Lee and O.L. Landen, Phys. Rev. E **67**, 026412 (2003).
10. M. Baus and J. Hansen, Phys. Rep. **59**, 1 (1980).
11. K. Wünsch, P. Hilse, M. Schlanges, and D.O. Gericke, Phys. Rev. E **77**, 056404 (2008).
12. K. Wünsch, J. Vorberger, and D.O. Gericke, Phys. Rev. E **79**, 010201(R) (2009).
13. J. Chihara, J. Phys. F: Met. Phys. **17**, 295 (1987).
14. J. Chihara, J. Phys.:Condens. Matter **12**, 231 (2000).
15. D. Kremp, M. Schlanges, and W.-D. Kraeft, *Quantum Statistics of Nonideal Plasmas* (Springer, Berlin, 2005).
16. R. Thiele *et al.*, Phys. Rev. E. **78**, 026411 (2008).
17. M.W.C. Dharma-wardana, Phys. Rev. A **45**, 45 (1992).
18. K. Wünsch, J. Vorberger, M. Schlanges and D.O. Gericke, J. Phys. (Conf. Series) **112**, 032077 (2008).
19. D.O. Gericke, J. Vorberger, K. Wünsch, and G. Gregori, Phys. Rev. E **81**, 065401(R) (2010).
20. J.P. Hansen and I.R. McDonald, *Theory of Simple Liquids* (Academic Press, London, 1990).